# Cerebrovascular damage caused by the gut microbe/host co-metabolite *p*-cresol sulfate is prevented by blockade of the EGF receptor

Sita N. Shah[1], Tobias B-A. Knausenberger[1], Matthew G. Pontifex[2], Emily Connell[2], Gwénaëlle Le Gall[2], Tom A. J. Hardy[1], David W. Randall[3,4], Kieran McCafferty[3,4], Muhammad M. Yaqoob[3,4], Egle Solito[4,5], Michael Müller[2], Andrew V. Stachulski[6], Robert C. Glen[7,8], David Vauzour[2], Lesley Hoyles[9]* & Simon McArthur[10]*†

[1] Blizard Institute, Faculty of Medicine & Dentistry, Queen Mary, University of London, 4, Newark Street, London, UK
[2] Norwich Medical School, Biomedical Research Centre, University of East Anglia, Norwich, UK
[3] Department of Renal Medicine and Transplantation, Royal London Hospital, Barts Health NHS Trust, London, UK
[4] William Harvey Research Institute, Faculty of Medicine & Dentistry, Queen Mary, University of London, John Vane Science Centre, Charterhouse Square, London, UK
[5] Dipartimento di Medicina Molecolare e Biotecnologie Mediche, Università degli Studi di Napoli Federico II, Naples, Italy
[6] Robert Robinson Laboratories, Department of Chemistry, University of Liverpool, Liverpool, UK
[7] Faculty of Medicine, Department of Metabolism, Digestion and Reproduction, Imperial College London, London, UK
[8] Centre for Molecular Informatics, Department of Chemistry, University of Cambridge, Cambridge, UK
[9] Department of Biosciences, School of Science and Technology, Nottingham Trent University, Clifton, Nottingham, UK
[10] Institute of Dentistry, Faculty of Medicine & Dentistry, Queen Mary, University of London, Blizard Institute, 4, Newark Street, London, UK

* Correspondence to Prof Lesley Hoyles (lesley.hoyles@ntu.ac.uk) or Dr Simon McArthur (s.mcarthur@qmul.ac.uk)
† Lead contact

**Running Title:** *p*-cresol sulfate damages the blood-brain barrier

**Abstract**

Circulating levels of the gut microbe/host co-metabolite p-cresol sulfate (pCS) correlate with cerebrovascular event risk in individuals with chronic kidney disease, but whether this relationship is mechanistic is unclear. We hypothesised that pCS would impair function of the blood-brain barrier (BBB), the primary brain-vasculature interface. We report that pCS exposure impairs BBB integrity in human cells *in vitro* and both acutely and chronically in mice, enhancing tracer extravasation, disrupting barrier-regulating tight junction components and ultimately affecting whole-brain transcriptomic activity. *In vitro* and *in vivo* mechanistic studies showed that pCS activated epidermal growth factor receptor (EGFR) signalling, resulting in matrix metalloproteinase mobilisation and BBB damage. Furthermore, blockade of EGFR prevented the permeabilising effects of serum from haemodialysis patients upon cerebromicrovascular endothelia *in vitro*. Our results define a pathway linking the co-metabolite pCS with BBB damage and suggest targeting the EGFR may mitigate against cerebrovascular damage in CKD.

**Keywords**

Blood-brain barrier, *p*-cresol sulfate, cerebrovascular disease, chronic kidney disease, gut microbiota

**Abbreviations:** BBB, blood–brain barrier; CKD, chronic kidney disease; EGFR, epidermal growth factor receptor; IS, indoxyl sulfate; MMP, matrix metalloproteinase; pCS, *p*-cresol sulfate; pCG, *p*-cresol glucuronide; SPIA, signalling pathway impact analysis; TEER, transendothelial electrical resistance; ZO-1, zonula occludens-1.

Communication between the commensal microbiota and host systems is implicated in many areas of health and disease[1], with substantial evidence highlighting gut microbes as modifiers of CNS function[2], but far less known about how these links are mediated[3]. Microbial modulation of afferent neural[4], immune[5] and neuroendocrine[6] activity has been described, but perhaps the least well characterised route of gut-brain communication is direct exposure to the myriad microbe-derived metabolites present in the circulation[7]. We and others have recently shown gut microbe-derived circulating metabolites (e.g. short-chain fatty acids[8,9] and methylamines[10]) to target the blood-brain barrier (BBB), but the impact of other gut microbial metabolites upon the brain vasculature, and their roles in health and disease, are largely unexplored.

One important microbe-derived metabolite given its links with kidney dysfunction is *p*-cresol, produced by fermentation of tyrosine and phenylalanine in the colon, particularly by *Coriobacteriaceae* or *Clostridium* species[11,12]. Luminal *p*-cresol undergoes extensive conjugation in both enterocytes[13] and the liver[14], such that it is found almost exclusively as *p*-cresol sulfate (pCS, ~90 % in humans) and *p*-cresol glucuronide (pCG) in the systemic circulation[15]. Normally, these molecules are efficiently cleared by the kidneys with an effective plasma half-life of ~30 min in rodents[16]. However, due to its high binding affinity to albumin, pCS accumulates within the plasma of individuals with compromised renal function[17] and is poorly removed by haemodialysis[18], a feature of significance given that increased plasma concentrations of pCS predict mortality in individuals with chronic kidney disease (CKD)[19,20].

CKD is a complex disorder affecting many aspects of physiology, but is notably associated with significant neurological and cerebrovascular complications[21]. Patients with CKD are at an increased risk of both ischaemic and haemorrhagic stroke, even after correcting for coincident vascular risk factors[22], and tend to have worse functional outcomes post-infarct[23], a major unmet clinical need[24]. Moreover, CKD is associated with both enhanced BBB permeability[25] and the presence of microbleeds[26], suggesting the cerebral vasculature is directly damaged in the condition.

These links between CKD and cerebrovascular disease, alongside reports from clinical studies associating plasma pCS and stroke risk[27] and experimental work showing pCS to induce dermal microvascular leakage[28] and aortic oxidative damage and remodelling[28,29], led us to hypothesise that this gut microbe-host co-metabolite directly damages the cerebral vasculature, impairing BBB function and contributing to the neurological consequences of CKD. Here, we report a clear deleterious effect of pCS upon BBB integrity, mediated through stimulation of the epidermal growth factor receptor (EGFR) and ensuing matrix metalloproteinases (MMPs) activation. Moreover, we show antagonism of the EGFR to prevent the BBB-permeabilising actions of serum from CKD patients, offering a potential new pathway to protect against uraemia-associated cerebrovascular damage linked to the actions of the gut microbiota.

## Results

*Treatment with pCS increases brain endothelial permeability in vitro and in vivo*

To assess the effects of pCS upon BBB integrity, we first examined its effects upon a simple *in vitro* model of BBB function, namely the paracellular permeability barrier of a monolayer of the immortalised human cerebromicrovascular endothelial line hCMEC/D3[30]. Treatment with pCS (24 h; 10 μM, 100 μM or 1 mM) significantly ($P < 0.05$) and dose-dependently enhanced permeability to a 70 kDa FITC-dextran tracer (Fig. 1A) and reduced trans-endothelial electrical resistance (TEER; Fig. 1B). Notably, pCS showed no signs of endothelial toxicity at any concentration tested (Extended Data Fig. 1) and given that pCS was administered as a potassium salt, equivalent concentrations of KCl had no effect on barrier function (Extended Data Fig. 1). Moreover, chelation of pCS by inclusion of 50 mg/ml human albumin (approximately equivalent to human serum concentrations[31]) blocked its effects on paracellular permeability and TEER (Extended Data Fig. 2). The BBB permeability barrier is underpinned by tight inter-endothelial junctions and their interactions with the actin cytoskeleton; hence, we examined the effect of pCS treatment upon the key tight junction component zonula occludens-1 (ZO-1) and fibrillar actin in hCMEC/D3 monolayers. In comparison with untreated cells, pCS exposure (24 h, 10 μM) markedly disrupted the marginal localisation of ZO-1 (Fig. 1C), as well as disrupting actin fibril arrangement itself (Fig. 1D), with a clear loss of cortical actin and appearance of trans-cytoplasmic fibres.

To confirm that these *in vitro* findings had relevance for whole animal physiology, we exposed male C57Bl/6 mice to pCS (10 mg/kg i.p., chosen to approximately double circulating free pCS concentrations[32]; 2 h, 6 h) before assessing BBB permeability through cerebral extravasation of the albumin-binding tracer Evans blue. Treatment of mice with pCS resulted in a significant ($P < 0.02$) increase in brain parenchymal Evans blue at both 2 h and 6 h post-administration (Fig. 1E).

CKD is characterised in part by persistently elevated circulating levels of pCS; hence we examined how continuous pCS release from implanted osmotic minipumps for four weeks affected the BBB, neuroinflammation and cognitive function (see Extended Data Table 1 for serum metabolite content analysis). Animals so exposed to pCS exhibited both significantly enhanced extravasation of the tracer sodium fluorescein into the brain parenchyma (Fig. 1F), and disrupted expression of the key BBB inter-endothelial tight junction molecules claudin-5 (Fig. 1G) and ZO-1 (Fig. 1H), confirming the deleterious effects seen with acute pCS administration. However, no obvious sign of microglial or astrocytic change were seen in the cortex of these animals (Extended Data Fig. 3), nor was performance in the open field test, Y-maze or novel object recognition task significantly affected (Extended Data Fig. 4) in comparison to saline-treated animals.

*Murine whole brain transcriptomic analysis reveals a suppressive effect of pCS exposure upon neuronal activity*

To investigate potential mechanisms of pCS action, we performed RNAseq analysis of whole-brain transcriptomes, comparing untreated and pCS-exposed mice (10 mg/kg i.p., 2 h). We found 380/16,988 genes assayed were significantly differentially expressed ($P < 0.05$, Benjamini-Hochberg): with 91 genes being significantly upregulated in the pCS-exposed group, while 289 were significantly downregulated (Fig. 2A; Extended Data Table 2). Among BBB-specific genes, the expression of *Slc1a2* ($\log_2$ fold change -1.35), *Adgra2* (1.03) and

151 *Serpini1* (-1.93) was found to be significantly changed ($P$ <2.66x10$^{-4}$ for all, Benjamini-
152 Hochberg).
153
154 Analysis of over-represented Gene Ontology categories within differentially expressed genes
155 using Enrichr[33] revealed that, while no categories associated with significantly up-regulated
156 genes reached statistical significance after multiple testing correction, several biological
157 processes and molecular functions associated with significantly ($P$ < 0.05; Benjamini-
158 Hochberg) down-regulated genes could be identified (Fig. 2B). Broadly, these fell into two
159 main categories: ontologies reflective of neuronal function and synaptic activity, and those
160 indicating intracellular protein translocation and metabolism. Signalling Pathway Impact
161 Analysis (SPIA) demonstrated inhibition of pathways associated with glutamatergic synapse,
162 circadian entrainment, and Alzheimer disease (pGFWER < 0.05; Table 1). Topological
163 analysis of the network generated from the 380 significantly differentially expressed genes
164 mapped onto KEGG pathways identified in SPIA (pGFdr < 0.05; Table 1) suggested that the
165 genes for *Prkacb*, *Homer1*, *Tardbp*, *Calm1*, *Calm3*, *Ppp3r1*, *Ppp3cb* and *Grm5* had most
166 control over the network (Fig. 2C; Extended Data Table 3). Manual curation of SPIA-
167 highlighted genes identified several broad categories of primarily down-regulated function:
168 neuronal activity, mitochondrial respiration, translation, cell cycle activity, and intracellular
169 $Ca^{2+}$- and other signalling pathways (Fig. 2C), overall depicting a generalised inhibitory effect
170 of pCS upon brain function.
171
172 *Permeabilising effects of pCS are mediated through the EGFR*
173 Although transcriptomic analysis did not suggest a clear candidate pathway for the actions of
174 pCS directly upon the cerebral vasculature, previous studies have indicated that it may interact
175 with the EGFR[34], hence we investigated the potential involvement of this receptor in the effects
176 of the metabolite upon the BBB. Initial studies of hCMEC/D3 cells confirmed EGFR expression
177 (Fig. 3A) and showed it to be phosphorylated at Tyr1068 within 15 min of 10 μM pCS
178 stimulation, phosphorylation that was maintained for at least 30 min (Fig. 3B). That this was a
179 direct effect of pCS was confirmed by inclusion of the EGFR-specific inhibitor erlotinib (2.5
180 μM, 10 min pre-treatment), which effectively prevented EGFR phosphorylation (Fig. 3C).
181
182 Considering these interactions, we investigated whether EGFR activation mediated the
183 permeabilising actions of pCS upon hCMEC/D3 cells. Pre-treatment with erlotinib (2.5 μM, 10
184 min pre-treatment) efficiently ablated the pCS-induced (10 μM, 24 h) increase in paracellular
185 permeability (Fig. 3D) and decrease in TEER (Fig. 3E). These functional effects were
186 paralleled by a reduction in pCS-stimulated disruption to the intracellular distribution of the
187 tight junction molecule ZO-1 (Fig. 3F) and to the actin cytoskeleton (Fig. 3G).
188
189 While erlotinib has high selectivity for the EGFR, it is not without off-target effects; hence, we
190 confirmed the centrality of this receptor in pCS action through use of targeted siRNA-mediated
191 knockdown. Treatment of hCMEC/D3 cells expressing any of three independent siRNA
192 sequences (knockdown efficiencies of 65.3 %, 56.7 % and 76.8 % respectively, Extended
193 Data Fig. 5) with pCS (10 μM, 24 h) had little effect on either paracellular permeability (Fig.
194 3H) or TEER (Fig. 3I). This was in marked contrast to cells that had been either mock
195 transfected or transfected with non-targeting siRNA negative control sequence, in which pCS
196 exposure significantly ($P$ < 0.05) increased paracellular permeability (Fig. 3H) and significantly
197 ($P$ < 0.05) decreased TEER (Fig. 3I), closely aligning with previous experiments.
198

199 *pCS stimulation of EGFR activates an ANXA1–STAT3–MMP signalling pathway*
200 EGFR is coupled to a number of intracellular signalling pathways, but one potentially relevant
201 target is the protein annexin A1 (ANXA1)[35], a molecule we have previously identified as a
202 major regulator of BBB function[36]. We therefore investigated whether this protein was involved
203 in the response to pCS. Initial experiments confirmed that ANXA1 underwent Tyr21
204 phosphorylation in response to pCS exposure (10 μM, 30 min; Fig. 4A) in an erlotinib-sensitive
205 manner (2.5 μM, 10 min pre-treatment; Fig. 4B). Using hCMEC/D3 cells stably bearing shRNA
206 sequences to ANXA1[10] (Extended Data Fig. 5), we further identified that exposure to pCS (10
207 μM, 24 h) significantly enhanced paracellular permeability in monolayers of wild-type and
208 scramble shRNA-bearing hCMEC/D3 cells, but that this response was notably absent in cells
209 transfected with ANXA1 shRNA sequences (Fig. 4C). Similarly, TEER was significantly ($P <$
210 $0.01$) reduced in wild-type and scramble shRNA-bearing hCMEC/D3 cells upon pCS
211 exposure, but not in ANXA1 shRNA transfected cells (Fig. 4D).
212
213 Both EGFR signalling and ANXA1 Tyr21 phosphorylation have been linked with the
214 transcription factor STAT3[37,38], hence we examined the impact of pCS exposure upon STAT3
215 activation. Exposure of hCMEC/D3 cells to pCS (10 μM) significantly ($P < 0.001$) enhanced
216 STAT3 Tyr705 phosphorylation within 15 min (Fig. 4E), an effect that was not seen in cells
217 pre-treated with erlotinib (2.5 μM, 10 min pre-treatment; Fig. 4F) and was attenuated or absent
218 in hCMEC/D3 cells bearing ANXA1 shRNA sequences (Fig. 4G). Notably, pre-treatment of
219 hCMEC/D3 cells with the selective STAT3 inhibitor C188-9 (5 μM, 30 min pre-treatment)
220 significantly ($P \leq 0.002$) reduced the effects of pCS exposure (10 μM, 24 h) upon both
221 paracellular permeability to a 70 kDa FITC-dextran tracer (Fig. 4H) and TEER (Fig. 4I).
222
223 *Inhibition of MMP2/9 activity prevents the permeabilising effects of pCS in vitro*
224 Activation of MMPs, particularly that of MMP-2 and MMP-9, is known to be downstream of
225 EGFR[34] and STAT3[39] activation, to be capable of damaging BBB permeability[40], and to be
226 associated with CKD[41], leading us to hypothesise that the permeabilising effects of pCS might
227 be mediated through these enzymes. Stimulation of hCMEC/D3 cells with pCS (10 μM, 24 h)
228 significantly ($P \leq 0.001$) increased MMP-2 and MMP-9 expression (Fig. 5A), a response
229 inhibited by pre-treatment with either the EGFR inhibitor erlotinib (2.5 μM, 10 min pre-
230 treatment) or the STAT3 inhibitor C188-9 (5 μM, 30 min pre-treatment; Fig. 5B). Analysis of
231 hCMEC/D3 conditioned medium by gelatin zymography confirmed that these pCS-induced
232 (10 μM, 24 h) increases in cellular MMP-2 and MMP-9 expression were mirrored by enhanced
233 gelatinase activity (Fig. 5C), an increase again sensitive to erlotinib pre-treatment (2.5 μM, 30
234 min prior to 10 μM pCS; Fig. 6D).
235
236 To judge the relevance of this increase in MMP activity to endothelial barrier integrity, we
237 investigated the effect of selective MMP inhibitors upon the actions of pCS. Pre-treatment of
238 hCMEC/D3 monolayers with either the selective MMP-2 inhibitor ARP 100 (12 nM, 15 min pre-
239 treatment) or the selective MMP-9 inhibitor JNJ0966 (440 nM, 15 min pre-treatment)
240 prevented the disruptive effects of pCS exposure (10 μM, 24 h) upon paracellular permeability
241 to a 70kDa FITC-dextran tracer (Fig. 5E, H), TEER (Fig. 5F, I) and intracellular distribution of
242 the tight junction anchor ZO-1 (Fig. 5G, J).
243
244 *pCS impairs BBB integrity through an EGFR–STAT3–MMP-9 pathway in vivo*
245 Having established the EGFR–ANXA1–STAT3–MMP-2/9 pathway as mediating the effects of
246 pCS upon endothelial cell barrier function *in vitro*, we sought to validate this pathway *in vivo*.

Examination of C57Bl/6 male mice exposed to elevated circulating pCS for 4 weeks (Extended Data Table 3) revealed a clear increase in brain blood vessel-associated MMP-9 (though not MMP-2) expression (Fig. 6A-B), confirming that at least a similar pathway to that seen in human cells is operative in mice. Furthermore, pre-treatment of male C57Bl/6 mice with the EGFR inhibitor erlotinib (50 mg/kg, i.p., 1 h pre-treatment) prior to pCS injection (10 mg/kg i.p., 2 h) suppressed the pCS-induced immunohistochemical appearance of Tyr21 phospho-ANXA1 (Extended Data Fig. 6) and MMP-9 (Fig. 6C-D) within the cerebrovascular wall, ameliorated pCS-induced disruption of vascular ZO-1 expression (Fig. 6E) and prevented a pCS-induced increase in parenchymal Evans blue tracer extravasation (Fig. 6F). Confirming the importance of pCS-induced MMP activity in mediating BBB disruption, pre-treatment of mice with the MMP-2/9 dual-specific inhibitor SB-3CT (10 mg/kg i.p., 1 h pre-treatment) also prevented pCS treatment (10 mg/kg i.p., 2h) from increasing parenchymal Evans blue extravasation (Fig. 6G).

*Treatment with the EGFR inhibitor erlotinib can prevent the permeabilising effect of CKD patient serum upon hCMEC/D3 monolayers*

While kidney failure is associated with damage to the cerebral vasculature, it is also associated with altered circulating levels of numerous uraemic retention molecules, of which pCS is only one, albeit important, example. Most notably, the EGFR has been demonstrated to interact with the gut microbe-derived uraemic toxin indoxyl sulfate (IS)[42], although treatment of hCMEC/D3 monolayers with this metabolite was without effect on paracellular permeability to a 70 kDa FITC-dextran tracer or TEER at any concentration tested (5 μM, 25 μM, 50 μM, 150 μM; Extended Data Fig. 7).

To investigate the relative importance of pCS in mediating the cerebrovascular symptoms of CKD, we exposed hCMEC/D3 monolayers for 24 h to medium containing 20 % de-complemented serum from individuals undergoing haemodialysis or age-matched individuals with normal kidney function who were undergoing evaluation as potential kidney donors (full patient details in Table 2), either alone or in combination with erlotinib (2.5 μM, 10 min pre-treatment). Treatment of hCMEC/D3 cells with haemodialysis patient sera, but not with that from healthy donors, significantly ($P = 0.004$) enhanced paracellular permeability to a 70 kDa FITC-dextran tracer, an effect reversed by erlotinib pre-treatment (Fig. 7A), although notably none of these treatments affected TEER (Fig. 7B). Additionally, similar treatment of hCMEC/D3 cells with sera from haemodialysis patients, but again not with that from healthy donors, significantly ($P < 0.05$) increased intracellular expression of both MMP-2 (Fig. 7C) and MMP-9 (Fig. 7D).

Having established that sera from individuals with kidney failure could modulate permeability of our *in vitro* BBB model in an erlotinib-sensitive manner, we examined the relative contributions of different amino acid-derived potential uraemic toxins to this response. Following analysis of serum concentrations of different metabolites by LC-MS/MS (Table 3; mean pCS concentrations: healthy donor 14.12 ± 3.09 μM, haemodialysis patient 155.26 ± 27.36 μM, $P<0.001$), we correlated these with changes in paracellular permeability; only correlations with pCS (rho = 0.675, $P_{FDR} = 0.01$; Fig. 7E) and the tryptophan metabolite xanthurenic acid (rho = 0.442, $P_{FDR} = 0.02$; Fig. 7F) remained significant following correction for multiple testing.

## Discussion

Impaired kidney function has serious consequences for virtually every organ system in the body, and the central nervous system is no exception. Patients with CKD, including those at not yet requiring dialysis, exhibit significant cognitive decline[43] and enhanced stroke risk[44], even after correction for typical cardiovascular risk factors. Cerebral microvascular disease and BBB disruption are thought to underlie these links[45], but little is known about how renal impairment results in BBB damage. Here we present data indicating a novel BBB-disruptive role for the major uraemic toxin and gut microbe-host co-metabolite pCS, acting *via* the EGFR to mobilise MMP activity. Moreover, we show that pCS treatment induces widespread transcriptomic changes within the brain, rapidly dampening numerous aspects of neuronal activity and metabolism. Together, these data strongly implicate pCS as a major contributory factor to the links between kidney failure and impaired brain function.

Interactions of pCS with the peripheral vasculature have previously been reported, with evidence of arterial leakage in patients with CKD[46] and in animal[28] and *in vitro* models of uraemia[47]. Mechanistically, pCS at concentrations found in uraemia can cause inter-endothelial adherens junction disruption[46], potentially underlying uraemia-associated endothelial leakage. Here, we extend the damaging actions of pCS to the cerebral vasculature and BBB *in vivo*, acting at concentrations similar to those of free pCS seen at stages III-IV of CKD[48]. We further provide mechanistic evidence coupling pCS agonism at the EGFR, *via* phosphorylation of ANXA1 and STAT3 to mobilisation of MMP activity, a known contributor to neurovascular disruption[49]. Importantly, these actions appear clinically relevant, with the serum of human haemodialysis patients impairing *in vitro* brain endothelial permeability barrier with a potency highly correlated to levels of pCS, an effect prevented by co-administration of the EGFR antagonist erlotinib. This positioning of the EGFR as a major mediator of pCS actions in the brain may additionally point to potential therapeutic strategies guarding against cerebrovascular damage in CKD; several EGFR inhibitors (e.g., erlotinib, gefitinib) and monoclonal antibodies (e.g., cetuximab, necitumumab) are licenced for clinical use in malignant disease, suggesting there may be scope for broader use in CKD, although caution is needed regarding the safety of at least some of these agents in advanced renal impairment[50]. Nonetheless, this highlights the possibility of developing an alternative risk-reduction strategy for cerebrovascular complications in CKD, something currently chiefly addressed through management of hypertension.

Cerebral small vessel disease, for which BBB failure is a fundamental driver[51], is thought to contribute to both the cognitive impairments and enhanced stroke risk seen in CKD patients[52]. What is less clear, partly due to the obscuring effects of the relationship between CKD and cerebrovascular risk factors such as diabetes and hypertension, is why this is the case. Activation of MMPs within the neurovascular unit has been reported in several forms of cerebrovascular disease, including stroke[53], traumatic injury[54], cerebral small vessel disease[55] and, notably, in murine models of CKD[56]. By elaborating a mechanistic link between gut microbe/host co-derived pCS, cerebrovascular MMP activity and impaired BBB integrity, we provide an explanation for how cerebral vessels may be damaged in CKD. Moreover, whilst local MMP activity has been demonstrated in a range of kidney disorders[57], whether this holds true in the brains of CKD patients is unknown. Our data indicating both a close correlation between pCS content and the BBB-permeabilising actions of haemodialysis patient serum, and moreover that exposure to such serum directly enhances endothelial MMP expression, suggest that this is highly likely.

While enhanced BBB permeability is a recognised driver of damage to cognitive function[58], our data suggest that the effects of pCS upon brain function extend beyond its immediate impact on the cerebral vasculature. Transcriptional analysis of pCS-exposed mice indicates a more generalised inhibitory effect of the toxin upon neural activity, which might also be expected to impair cognitive abilities. We did not detect such cognitive disruption following long-term pCS exposure however, a finding with several potential explanations. Previous studies identifying cognitive sequelae of BBB damage have shown a substantial increase in permeability, in the order of a 5 fold increase or greater[59,60], to be associated with cognitive deficits. In our study, animals exposed for one month to pCS exhibited an approximately 30% increase in tracer permeability across the BBB; it may be that the degree of permeability deficit caused in this study was insufficient to impair cognition to a degree detectable using the tests employed. Notably, previous studies employing higher pCS concentrations have shown the metabolite to impair cognition in both humans[61] and mice[59].

Intriguingly, while pCS clearly influenced BBB permeability, we found no evidence that this was true for the other major gut microbe-derived uraemic toxin, IS. This is perhaps surprising, given previous evidence that IS concentrations correlate with BBB impairment in partially nephrectomised ratsz[59] and vascular disease in CKD patients[62]. In contrast, however, suppression of raised circulating IS by sequestration did not reverse adenine-rich diet induced BBB impairment[59], highlighting the complexity of the pathways impinging on the BBB. Taken alongside our recent demonstration that the CKD-associated molecule trimethylamine *N*-oxide (TMAO) exerted marked beneficial effects upon both the BBB and cognition at levels seen in metabolically healthy individuals[10], it appears the generalised assumption that uraemia-associated molecules are always deleterious may need revisiting[63].

While pCS predominates in the circulation, it is not the only *p*-cresol conjugate found in blood, with pCG representing a significant, albeit minor, fraction[15]. Moreover, levels of pCG do increase markedly with worsening CKD stages, and have been shown to correlate with mortality risk in a similar way to pCS[64]. However, we have shown pCG to exert very different actions upon the BBB to pCS, with its administration at physiologically relevant levels *in vivo* enhancing barrier integrity by antagonism of basal circulating lipopolysaccharide interactions with TLR4[65]. Moreover, whole brain RNAseq analysis of pCG-exposed mice indicated a positive regulation in neuronal activity gene ontologies, notably opposite to the suppressive effects of pCS described here[65]. That the two major conjugates of gut microbe-derived *p*-cresol should so markedly differ in effect upon the brain is striking, emphasising the need for mechanistic studies of gut microbe/host co-metabolite action before conclusions can safely be drawn about their clinical role(s).

Most circulating pCS is ultimately derived from the actions of gut microbes upon dietary amino acids[11], thus our description of its effects upon the BBB further emphasises the importance of this facet of gut microbe-host interactions. Notably, while we and others have shown other gut microbe-derived metabolites, including short-chain fatty acids[8,9], methylamines[10], and pCG[65] to reinforce BBB integrity in healthy animals, pCS is overtly detrimental in its effects. Given the wide range of metabolites produced by gut microbes, that some agents are deleterious at supraphysiological concentrations is unsurprising, but does emphasise the importance of mechanistic analyses of gut-brain communication pathways. Overall, our description of pCS as a major link between gut microbes, kidney function and the cerebral vasculature highlights

390 the role of the gut microbiota in at least some of the systemic effects of renal disease,
391 emphasising its potential as a therapeutic target for clinical management of CKD.
392

## Methods

*Human serum samples*

Pre-dialysis serum samples were collected from patients undergoing haemodialysis at Barts Health NHS Trust and from age-/sex-matched healthy controls undergoing evaluation for kidney donation who had previously consented for sample inclusion in the Barts Diabetic Kidney Disease Biobank, see Table 2 for demographic details. Ethical approval for the inclusion in the Barts DKC Biobank was provided under REC reference no. 18/EE/0142. Approval for the current study was provided under REC reference no. 20/LO/0361. The study followed established standard operating procedures and all experiments involving human tissue conformed to the principles set out in the World Medical Association Declaration of Helsinki. All serum samples were de-complemented by incubation at 56 °C for 20 min prior to use.

*Animals*

Wild-type, male, specific pathogen-free, C57Bl/6J mice (Charles River UK Ltd., Margate, UK) were used for all experiments, aged between 7 and 8 weeks at the start of experiments. All experiments were approved by the QMUL Animal Welfare and Ethical Review Board (acute studies) or the University of East Anglia Animal Welfare and Ethical Review Body (long-term studies) and were performed in accordance with the ARRIVE guidelines and the UK Animals (Scientific Procedures) Act, 1986, under UK Home Office Project Licences PFA5C4F4F and PP9417531. Individual animals were used as experimental units; animals were randomly assigned to groups using the =rand() function of Microsoft Excel.

*Animals: acute studies*

Mice were housed in groups of five per cage in a room with controlled lighting (lights on 08.00–20.00 h) and temperature (21–23 °C) and with standard lab chow (5058, LabDiet, St. Louis, USA) and water available *ad libitum.* Mice were acclimatised to the animal facility environment for one week prior to experimentation, randomised to treatment group, treated as described below, and killed by transcardial perfusion with ice-cold 0.1 M phosphate buffered saline (PBS) under deep sodium pentobarbital anaesthesia (50 mg/kg, i.p.). Whole blood was collected and permitted to coagulate for 30 minutes at room temperature, prior to centrifugation at 800g for separation of serum, and brains were rapidly removed and bisected. For immunohistochemical analysis, half-brains were fixed by immersion in 4 % formaldehyde in 0.1 M PBS at 4 °C for 24 h, after which they were embedded in paraffin wax. For RNAseq studies, half-brains were stored in RNAlater (ThermoFisher Scientific Ltd., UK) at 4 °C overnight, and then frozen at -80 °C for later RNA extraction as described below. For studies of Evans blue dye extravasation, half-brains were collected into 0.1 M phosphate buffered saline (PBS) at 4 °C for later analysis as described below. In all cases, further tissue analysis was performed blinded to original groupings.

*Animals: long-term studies*

Mice were housed in groups of four per cage in a room with controlled lighting (lights on 08.00–20.00 h) and temperature (21–23 °C) and with standard lab chow (5058, LabDiet, St. Louis, USA) and water available *ad libitum*. Mice were acclimatised to the animal facility environment for two weeks prior to experimentation. Animals were anaesthetised by isofluorane inhalation and subcutaneously implanted with osmotic minipumps (model 2004, Alzet Cupertino, CA, USA) previously loaded with either 30 mg/ml pCS or saline vehicle, designed to release contents at 0.25 µl/h for a total period of 4 weeks, with minipump contents assigned randomly

441 across groups. At the end of this period mice were killed by transcardial perfusion with ice-
442 cold 0.1 M phosphate buffered saline (PBS) under deep sodium pentobarbital anaesthesia
443 (50 mg/kg, i.p.). Whole blood was collected and permitted to coagulate for 30 minutes at room
444 temperature, prior to centrifugation at 800g for separation of serum, and brains were rapidly
445 removed and bisected. For immunohistochemical analysis, half-brains were fixed by
446 immersion in 4 % formaldehyde in 0.1 M PBS at 4 °C for 24 h, after which they were embedded
447 in paraffin wax. For studies of sodium fluorescein extravasation, half-brains were collected into
448 0.1 M phosphate buffered saline (PBS) at 4 °C for later analysis as described above. In all
449 cases, further tissue analysis was performed blinded to original groupings.
450
451 *In vivo BBB permeability analysis*
452 Mice were injected i.p. with 100 µl of a 2 % w/v solution of Evans blue tracer in 0.9 % saline
453 (Merck Ltd, Poole, UK) or i.v. with 200 µl of a 2% w/v solution of sodium fluorescein in 0.9 %
454 saline (Merck Ltd., UK). Tracer was permitted to circulate for 1 h before animals were deeply
455 anaesthetised with sodium pentobarbital (50 mg/kg, i.p.) and, following sampling of blood by
456 cardiac puncture, transcardially perfused with 0.9 % PBS at 4 °C to remove dye remaining
457 within the vasculature. Brains were removed, bisected and left hemispheres were
458 homogenised by maceration in 0.1 M PBS. Suspended macromolecules were precipitated by
459 incubation with 60 % trichloroacetic acid, and tracer content of the resulting supernatants was
460 assessed using a CLARIOstar fluorescence spectrophotometer, set to read absorbance at
461 620 nm for Evans blue, or fluorescence at 516 nm for sodium fluorescein (BMG Labtech
462 GmbH, Germany) alongside a standard curve of defined concentrations of tracer in the same
463 buffer. Brain tracer content was expressed as µg of dye/mg of brain tissue, normalised to
464 circulating serum concentrations.
465
466 *RNAseq analysis*
467 Mice were transcardially perfused with 0.9 % saline at 4 °C to remove circulating blood, and
468 brains were removed and collected into RNAlater (Thermofisher Scientific Ltd., UK) prior to
469 storage at -20 °C for later analysis. Whole brain total RNA was extracted using a PureLink
470 RNA Mini Kit (Thermofisher Scientific Ltd., UK) and quantified using a CLARIOstar
471 spectrophotometer equipped with an LVis microplate (BMG Labtech GmbH, Germany). RNA
472 samples ($n$ = 5 pCS, $n$ = 5 saline control) were sent to Macrogen Inc. (Republic of Korea)
473 where they were subject to quality checks (RIN analysis); libraries were prepared (TruSeq
474 Stranded mRNA LT Sample Prep Kit) for paired-end (2× 100 nt) sequencing on an Illumina
475 HiSeq 4000 apparatus. Raw RNAseq sequence data (delivered in fastq format) were
476 processed in-house as follows. Single-end forward reads were mapped onto the mouse
477 genome (mm10) using HISAT2 v2.2.1[66]. The number of reads in each sample that mapped to
478 exons in the BAM files returned by HISAT2 was determined using featureCounts within
479 subread v2.0.1[67]. DESeq2 v1.34.0[68] was used to identify significantly ($P < 0.05$, Benjamini-
480 Hochberg) differentially expressed genes in the dataset. Entrez gene identifiers were
481 converted to gene symbols using *Mus musculus* annotations downloaded from NCBI on 12
482 October 2022. Enrichr[33] was used to perform Gene Ontology analysis. SPIA v2.48.0[69] was
483 used to identify KEGG pathways inhibited or activated in mouse brain samples exposed to
484 pCS. KEGGgraph v1.56.0[70] was used to generate the topological network from the $\log_2$ fold
485 change values for the significantly differentially expressed genes and KEGG xml files for the
486 *Mus musculus* pathways of interest. igraph v1.3.5[71] was used to generate summary network
487 statistics. Raw RNAseq data have been deposited with ArrayExpress under accession number
488 E-MTAB-12326.

*Immunohistochemistry*

Paraffin-embedded brains were sectioned (5 µm) using a rotary microtome and collected onto glass microscope slides. Following deparaffinisation with xylene and rehydration using graded ethanol:water solutions, heat-mediated antigen retrieval was performed by incubation in 10 mM Tris base, 1 mM EDTA, 0.05 % Tween-20, pH 9.0 at 90 °C for 20 min. Once cooled, endogenous peroxide activity was quenched by incubation for 15 min in 0.3 % $H_2O_2$ in Tris-buffered saline (TBS; 50 mM Tris base, 150 mM NaCl, pH 7.4). Sections were permeabilised by incubation in TBS containing 0.025 % Triton X-100 for 10 min, blocked by incubation in 10 % normal goat serum in TBS for 30 min and treated with primary antibodies overnight at 4 °C (MMP2: rabbit anti-human, 1:1000 Insight Biotechnology Ltd., UK, MMP9: mouse anti-human, 1:50, Santa Cruz Biotechnology Inc, USA, phosphotyrosine-21 ANXA1: rabbit anti-human, 1:1000[72], ZO-1: rabbit anti-human 1:100, Thermofisher Scientific, UK), diluted in TBS containing 1 % normal goat serum, 0.025 % triton X-100, pH 7.4). Sections were washed thoroughly with TBS containing 1 % normal goat serum and incubated with relevant secondary antibody for 1 h at room temperature (horseradish peroxidase-conjugated goat anti-rabbit or anti-mouse 1:500, both Stratech Scientific, UK, AF488-conjugated goat anti-rabbit or anti-mouse 1:500, both Thermofisher Scientific, UK; diluted in TBS containing 1 % normal goat serum, 0.025 % triton X-100, pH 7.4). Sections were thoroughly washed in TBS and where appropriate peroxidase staining was developed using 0.5 mg/ml diaminobenzidine hydrochloride and 0.01 % $H_2O_2$. Sections were counterstained with haematoxylin or 50 ng/ml 4′,6-diamidino-2-phenylindole (DAPI) as appropriate and mounted for microscopic examination. Brightfield images were captured using a using a Nikon Eclipse 80i Stereology Microscope fitted with an Optronics Camera, using a 40x objective (NA: 0.75 mm, working distance: 0.66 mm). Fluorescence images were captured with an LSM880 confocal laser scanning microscope (Carl Zeiss Ltd., Cambridge, UK) fitted with 405, 488 and 561 nm lasers and an ×63 oil immersion objective lens (NA: 1.4 mm, working distance: 0.17 mm), using ZEN imaging software (Carl Zeiss Ltd., UK). All images were analysed with ImageJ 1.53 k software (National Institutes of Health, USA).

*Behavioural analyses*

Behavioural tests were performed in the order they are introduced below. Apparatus was cleaned using 70 % ethanol upon completion of each trial, eliminating any residual odour.

Open field test (OFT) was conducted as previously described[10]. Briefly, mice were placed in the centre of the OFT, a grey 50 x 50 x 50 cm apparatus illuminated with low lux (100 lux) lighting. Total travel distance and time spent in the centre of the field was determined at 5 min with a video tracking system (Smart 3.0 tracking software, Panlab, Kent, UK).

Y-maze spontaneous alternation test, a measure of spatial working memory, was performed on the final day of behavioural testing as previously described[10]. Briefly, the Y-maze apparatus comprised white Plexiglas (dimensions 38.5 × 8 × 13 cm, spaced 120° apart) and was illuminated with low lux (100 lux) lighting. Mice were placed in the maze and allowed to explore freely for 7 min while tracking software recorded zone transitioning and locomotor activity (Smart 3.0 tracking software, Panlab, Kent, UK). Spontaneous alternation was calculated using the following formula: Spontaneous Alternation = (Number of alternations/ Total Arm entries - 2) x 100.

537 The novel object recognition (NOR), a measure of recognition memory, was performed as
538 described previously[10]. Briefly, on day 1 mice were habituated in a grey 50 x 50 x 50 cm
539 apparatus illuminated with low lux (100 lux) lighting, mice were placed into the empty maze
540 and allowed to move freely for 10 min. On day 2, mice were conditioned to a single object for
541 a 10 min period. On day 3, mice were placed into the same experimental area in the presence
542 of two identical objects for 15 min, after which they were returned to their respective cages
543 and an inter-trial interval of 1 h was observed. One familiar object was replaced with a novel
544 object. Mice were placed back within the testing area for a final 10 min. Videos were analysed
545 for a 5 min period, after which if an accumulative total of 15 s with both objects failed to be
546 reached, analysis continued for the full 10 min or until 15 s was achieved. Those not achieving
547 15 s were excluded from the analysis[73]. A discrimination index (DI) was calculated as follows:
548 DI = (TN−TF)/(TN+TF), where TN is the time spent exploring the novel object and TF is the
549 time spent exploring the familiar object.
550
551 *Cell culture*
552 The human cerebromicrovascular endothelial cell line hCMEC/D3 was maintained and treated
553 as described previously[9]. Cells were cultured to confluency in complete endothelial cell growth
554 medium MV2 (PromoCell GmbH, Germany), whereupon VEGF was removed, and cells were
555 further cultured for a minimum of 4 days to enable intercellular tight junction formation prior to
556 experimentation. All cell cultures were used at passages 28-33 to ensure retention of
557 appropriate endothelial characteristics[30].
558
559 *In vitro barrier function assessments*
560 Paracellular permeability and TEER were measured on 100 % confluent hCMEC/D3 cultures
561 polarised by growth on 24-well plate polyethylene terephthalate (PET) transwell inserts
562 (surface area: 0.33 $cm^2$, pore size: 0.4 µm; Appleton Woods, UK) previously coated with calf-
563 skin collagen (15 µg/$cm^2$ and fibronectin 3 µg/$cm^2$; both Sigma-Aldrich, UK). The permeability
564 of hCMEC/D3 cell monolayers to 70 kDa FITC-dextran (2 mg/ml) was measured as described
565 previously[10]. TEER measurements were performed using a Millicell ERS-2 Voltohmmeter
566 (Millipore, Watford, UK) and were expressed as Ω.$cm^2$. In all cases, values obtained from cell-
567 free inserts similarly coated with collagen and fibronectin were subtracted from the total
568 values.
569
570 *Immunofluorescence analysis*
571 hCMEC/D3 cells were cultured on Lab-Tek™ Permanox™ 8-well chamber slides coated with
572 calf skin collagen (Sigma-Aldrich, UK), prior to immunostaining according to standard
573 protocols[74] and using a primary antibody directed against zona occludens-1 (ZO-1; 1:100,
574 Thermofisher Scientific, UK) or AF488-conjugated phalloidin (0.165 µM, Thermofisher
575 Scientific, UK). Nuclei were counterstained with DAPI (Sigma-Aldrich, UK). Images were
576 captured using an LSM880 confocal laser scanning microscope (Carl Zeiss Ltd., Cambridge,
577 UK) fitted with 405, 488 and 561 nm lasers and a × 63 oil immersion objective lens (NA, 1.4
578 mm, working distance, 0.17 mm). Images were captured with ZEN imaging software (Carl
579 Zeiss Ltd., UK) and analysed using ImageJ 1.53k (National Institutes of Health, USA).
580
581 *Flow cytometry*
582 Following experimental treatment, hCMEC/D3 cells were detached from growth surfaces as
583 described previously[9], washed in 0.1 M PBS at 4 °C and fixed by incubation for 15 min at room
584 temperature in 4 % formaldehyde in 0.1 M PBS. For analysis of intracellular phospho-ANXA1,

585 phospho-EGFR or phospho-STAT3 cells were then permeabilised by incubation for 10 min in
586 ice-cold 90 % methanol in 0.1 M PBS. Cells were then incubated at 4 °C for 20 min with 10 %
587 fetal calf serum in 0.1 M PBS, 1 mM $CaCl_2$ for 20 min to block non-specific secondary antibody
588 binding; blocking buffer was further supplemented with 0.05 % Triton X-100 to permeabilise
589 cells used for analysis of total EGFR, ANXA1, MMP2 or MMP9. Cells were then incubated
590 with primary antibodies raised against, variously, ANXA1 (rabbit anti-human, 1:1000,
591 ThermoFisher Scientific, UK), phosphotyrosine-21 ANXA1 (rabbit anti-human, 1:1000[72]),
592 EGFR (rabbit anti-human, 1:50, Cell Signalling Technologies, UK), phosphotyrosine-1068
593 EGFR (mouse anti-human, 1:1000, Cell Signalling Technologies, UK), MMP2 (rabbit anti-
594 human, 1:500, Insight Biotechnology Ltd, UK), MMP9 (mouse anti-human, 1:50, Santa Cruz
595 Biotechnology Inc., USA) or phosphotyrosine-705 STAT3 (mouse anti-human, 1:200, Cell
596 Signalling Technologies, UK) in 1 % FCS in 0.1 M PBS for 20 min on ice. Cells were washed
597 and incubated with either an AF488-conjugated goat anti-rabbit or an AF488-conjugated goat
598 anti-mouse secondary antibody as appropriate (1:300, Thermo-Fisher Scientific, UK) in 1 %
599 FCS, 0.1 M PBS for 20 min on ice. Immunofluorescence was analysed for 10,000 singlet
600 events per treatment using a BD FACSCanto II (BD Biosciences, UK) flow cytometer, with
601 resultant data being analysed with FlowJo 8.0 software (Treestar Inc., CA, USA).
602
603 *Gelatinase activity analysis*
604 hCMEC/D3 cells grown on 12-well plates were cultured to confluence in complete endothelial
605 cell growth medium MV2 (PromoCell GmbH, Germany), whereupon serum was removed and
606 cells were subjected to experimental treatment as described. Cell-free medium was collected
607 and concentrated 10-fold by centrifugal filtration (30 kDa cut-off, Pall Corporation, UK) at
608 14,000 g for 8 min, with resuspension in sterile 0.1 M PBS. Concentrated samples (10
609 µl/sample) were mixed with 5x non-reducing sample buffer (125 mM Tris.HCl, 4 % sodium
610 dodecyl sulfate (SDS), 20 % glycerol, 0.01 % bromophenol blue, pH 6.8; all Merck, UK) and
611 separated by gel electrophoresis (7.5% acrylamide, 4 mg/ml porcine gelatin; Merck, UK). SDS
612 was removed by washing in 50 mM Tris.HCl, 2.5 % Triton X-100, 5 mM $CaCl_2$, 1 µM $ZnCl_2$,
613 pH 7.5. Gelatinase activity was determined by incubation for 24 h in 50 mM Tris.HCl, 1 %
614 Triton X-100, 5 mM $CaCl_2$, 1 µM $ZnCl_2$, pH 7.5 followed by Coomassie staining (0.5 %
615 Coomassie brilliant blue, 40 % methanol, 10 % acetic acid). Gels were visualised using a
616 ChemiDoc MP Imaging System (Bio-Rad Laboratories Ltd., UK). Integrated optical densities
617 were calculated using NIH ImageJ 1.53k (National Institutes of Health, USA).
618
619 *EGFR siRNA*
620 hCMEC/D3 cells grown on 24-well plate polyethylene terephthalate (PET) transwell inserts
621 (surface area: 0.33 $cm^2$, pore size: 0.4 µm; Appleton Woods, UK) previously coated with calf-
622 skin collagen (15 µg/$cm^2$ and fibronectin 3 µg/$cm^2$; both Sigma-Aldrich, UK), were transfected
623 with one of three different commercial siRNA sequences designed to target the EGFR or an
624 Allstars negative control siRNA sequence (final concentration 1 nM; all Qiagen Ltd., UK) using
625 INTERFERin transfection reagent according to the manufacturer's instructions (Polyplus
626 Transfection, France), alongside mock transfected cells. After 96 h, cells were analysed for
627 TEER and paracellular permeability to a 70 kDa FITC-dextran tracer as described above. A
628 proportion of cells were analysed for EGFR expression by flow cytometry as described above
629 (Extended Data Fig. 5).
630
631 *ANXA1 shRNA*

632 hCMEC/D3 cells bearing shRNA sequences targeting ANXA1 or a scramble sequence were
633 used as described previously[10]. Prior to use, reduction in ANXA1 expression was confirmed
634 by flow cytometry as described above (Extended Data Fig. 5).
635
636 *Cell survival analysis*
637 The potential for pCS-induced cytotoxicity was assessed using the MTT assay. Briefly, cells
638 were treated with pCS (10 µM, 100 µM, 1 mM) for 24 h, prior to administration of MTT (3-(4,5-
639 dimethylthiazol-2-yl)-2,5-diphenyltetrazolium bromide; Merck Life Science UK Ltd.,
640 Gillingham, UK) at 500 µg/ml. Cells were incubated at 37 °C for 2 h, medium was removed
641 and resulting crystals were solubilised by incubation for 2 min in dimethyl sulfoxide.
642 Absorbance was read at 540 nm using a CLARIOstar spectrophotometer (BMG Labtech,
643 Ortenberg, Germany), with a reference wavelength at 570 nm.
644
645 *LC-MS/MS*
646 Serum samples were diluted with methanol at a ratio of 1:10 (v/v) and placed on dry ice for 10
647 min. Samples were then centrifuged (5 min, 16,000 *g* at room temp), supernatants filtered
648 using a 0.45 µm PTFE syringe filter and evaporated to dryness using a Savant™ SpeedVac™
649 High-Capacity Concentrator (Cat. SC210A-230). Dried samples were resuspended in 50 µl of
650 water with 15 µl of L-tryptophan-2,3,3-$d_3$ and *p*-toluenesulfonic acid at 50 µg/ml as the internal
651 standards for tryptophan and *p*-cresol metabolites, respectively.
652
653 Stock solutions of each metabolite were prepared in methanol (1 mg/ml) and stored at -80 °C.
654 Calibration standards were prepared by pooling all analytes at eight different concentrations
655 and adding the respective internal standards at 50 µg/ml. Calibration standards were run at
656 the beginning, middle and end of each analytical queue.
657
658 Two microlitres of the prepared sample was injected and separated using a Waters Acquity
659 UPLC system and Xevo TQ-S Cronos mass spectrometer and ACQUITY UPLC BEH C18 1.7
660 µm (2.1 x 50 mm) column. The electrospray ionisation operated in positive mode and
661 chromatic separation occurred using a 0.3 ml/min and composition of eluent A (0.1 % formic
662 acid, water) and eluent B (0.1 % formic acid, methanol) at a gradient of 5 % B from 0 to 0.5
663 min, 5 %-10 % B from 0.5 to 2.5 min, 10 %-15 % B from 2.5-3.5 min, 15 %-35 % B from 3.5
664 to 4.5 min, 35 % to 45 % B from 4.5 to 6.5 min, 45 % to 55 % B from 6.5 to 7 min, 55 % to 100
665 % B from 7 to 7.5 min, 100 % B until 10 min, and 5 % B from 10 to 10.1 min to return to initial
666 conditions for equilibration until 14 min. The analyte:internal standard response ratio was used
667 to create a calibration curve and quantify each metabolite.
668
669 Sample sizes were calculated to detect differences of 15 % or more with a power of 0.85 and
670 α set at 5 %, calculations being informed by previously published data[10]. Experimental data
671 are expressed as mean ± SEM, with n = 4-9 independent experiments for *in vitro* studies and
672 n=6-10 individual animals for *in vivo*/*ex vivo* studies, see figure legends for details of individual
673 experiments. For *in vivo*/*ex vivo* studies, individual animals were randomly assigned to groups
674 using the =rand() function of Microsoft Excel. Statistical analyses were performed using
675 RStudio 2022.07.1. In all cases, normality of distribution was established using the Shapiro–
676 Wilk test, followed by analysis with two-tailed Student's *t*-tests to compare two groups or, for
677 multiple comparisons, one- or two-way ANOVA with Tukey's HSD *post hoc* test as appropriate.
678 A *P* value of <5 % was considered significant.
679

**Acknowledgements**

This work was funded by Alzheimer's Research UK Pilot Grant No. ARUK-PPG2016B-6. This project has received funding from the European Union's Horizon 2020 research and innovation programme under grant agreement No 874583. This publication reflects only the authors' views, and the European Commission is not responsible for any use that may be made of the information it contains. The funders had no role in the study design, data collection or analysis, decision to publish, or preparation of the manuscript.

**Author Contributions**

Conceptualisation: LH, SM; Investigation: SNS, TBAK, MGP, EC, GLG, TAJH DV, LH and SM; Resources: DWR, KM, MMY and ES; Writing – original draft: SM; Writing – review & editing: MM, AVS, RCG, DV, LH and SM; Project administration: SM. All authors read and approved the final version of the manuscript.

**Declaration of Interests**

The authors declare no competing interests.

697 **Figure Legends**
698
699 **Figure 1: Exposure to pCS increases permeability of human cerebromicrovascular**
700 **endothelial cells *in vitro* and the murine BBB *in vivo*.** a) Incubation of hCMEC/D3 cell
701 monolayers with pCS (10 µM, 100 µM, 1 mM; 24 h) dose-dependently increased paracellular
702 permeability to a 70 kDa FITC-dextran conjugate; data are mean ± s.e.m., n = 9 independent
703 experiments. b) Incubation of hCMEC/D3 cell monolayers with pCS (10 µM, 100 µM, 1 mM;
704 24 h) dose-dependently reduced TEER; data are mean ± s.e.m., n = 9 independent
705 experiments. c, d) Confocal microscopic analysis of expression of c) AF488-phalloidin labelled
706 actin filaments (white) or d) the tight junction component zona occludens-1 (ZO-1; white) in
707 hCMEC/D3 cells following treatment for 24 h with 10 µM pCS, nuclei are counterstained with
708 DAPI (blue), scale = 15 µm. Images are representative of at least three independent
709 experiments. e) Treatment of male C57Bl/6 mice by i.p. injection of pCS (10 mg/kg) caused a
710 time-dependent increase in extravasation of Evans blue tracer into the CNS parenchyma,
711 reaching statistical significance at both 2 h and 6 h post administration; data are mean ± s.e.m.,
712 n = 5-6 animals. f) Exposure of male C57Bl/6 by s.c. implantation with osmotic mini-pumps
713 releasing pCS at 7.5 µg/h for 28 days significantly enhanced extravasation of sodium
714 fluorescein into the brain parenchyma; data are mean ± s.e.m., n = 7-10 animals. g, h)
715 Confocal microscopic analysis of expression of g) claudin-5 or h) zonula occludens-1 (ZO-1)
716 in the brains of male C57Bl/6 exposed by s.c. implantation with osmotic mini-pumps releasing
717 pCS at 7.5 µg/h for 28 days, nuclei are counterstained with DAPI (blue), scale = 10 µm. Images
718 are representative of 7-10 animals.
719
720

Figure 1

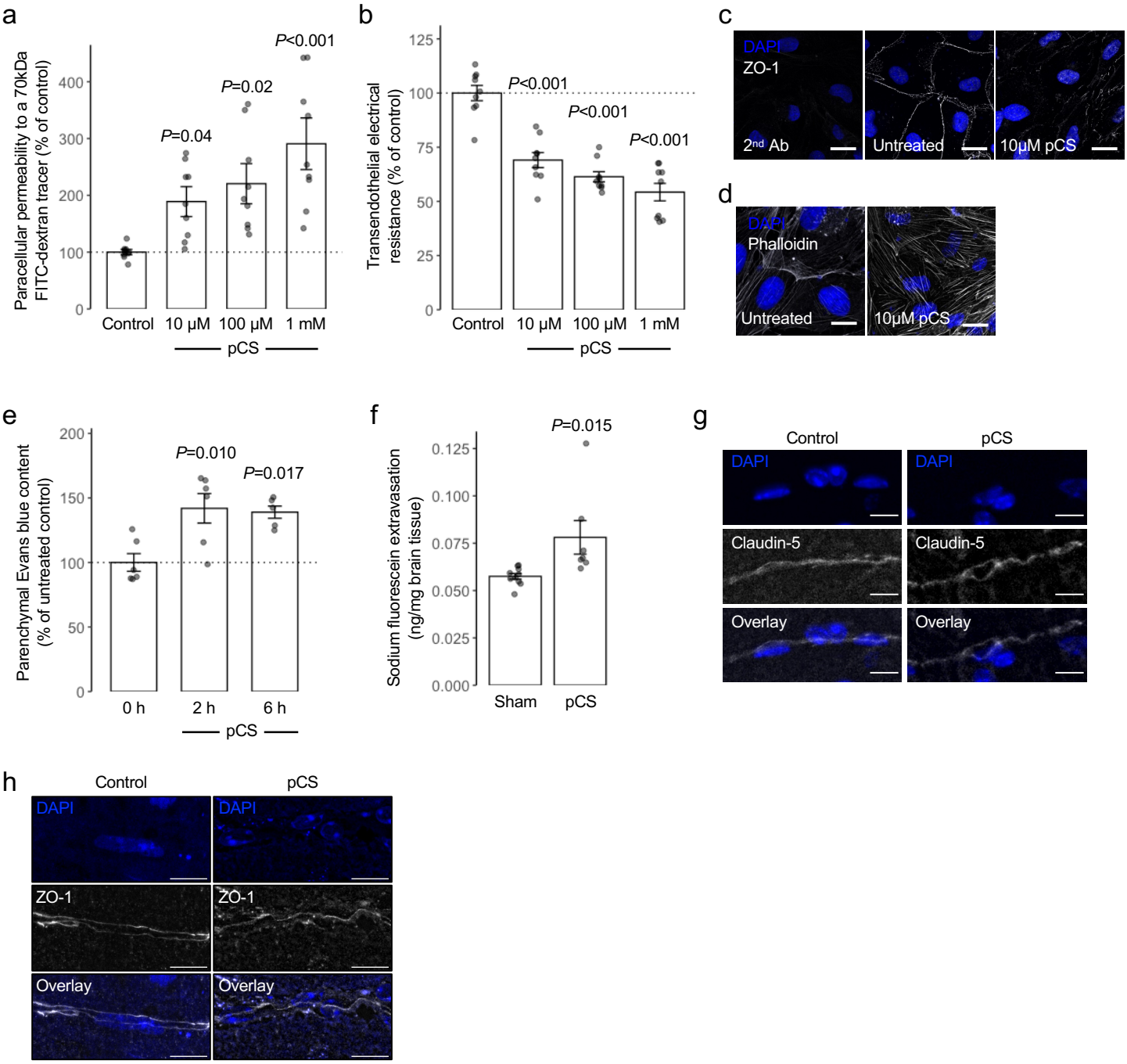
a
Paracellular permeability to a 70kDa FITC-dextran tracer (% of control)
P=0.04
P=0.02
P<0.001
Control
10 μM
100 μM
1 mM
pCS
b
Transendothelial electrical resistance (% of control)
P<0.001
P<0.001
P<0.001
Control
10 μM
100 μM
1 mM
pCS
c
DAPI
ZO-1
2nd Ab
Untreated
10μM pCS
d
DAPI
Phalloidin
Untreated
10μM pCS
e
Parenchymal Evans blue content (% of untreated control)
P=0.010
P=0.017
0 h
2 h
6 h
pCS
f
Sodium fluorescein extravasation (ng/mg brain tissue)
P=0.015
Sham
pCS
g
Control
pCS
DAPI
Claudin-5
Overlay
h
Control
pCS
DAPI
ZO-1
Overlay

721 **Figure 2: Exposure of mice to pCS for 2 h significantly affects brain gene expression.**
722 a) Volcano plot showing the 380 significantly differentially expressed genes among the 16,988
723 mouse genes examined in this study (n = 5 animals per group (treated, negative control)).
724 Black data points: no significant change in expression; red dots, significantly ($P < 0.05$,
725 Benjamini-Hochberg) upregulated expression in the pCS group compared with the negative
726 control; blue dots, significantly ($P < 0.05$, Benjamini-Hochberg) downregulated expression in
727 the pCS group compared with the negative control; n=5 per group. b) Biological processes
728 (above) and molecular functions (below) of genes found to be significantly downregulated (n=
729 289) upon exposure of mice to pCS, based on Enrichr *P* value ranking from Gene Ontology
730 analysis. c) Topological analysis of the KEGG network resulting from mapping the 380
731 significantly ($P < 0.05$, Benjamini-Hochberg) differentially expressed genes onto the 17 KEGG
732 *Mus musculus* metabolic pathways listed in Table 1. Blue solid circles, genes whose
733 expression is significantly downregulated in the pCS group compared with the control; red
734 solid circles, genes whose expression is significantly upregulated in the pCS group compared
735 with the control. Thick outline colours around the solid circles correspond to the molecular
736 functions listed in the legend. Network summary statistics are available in Table S3.
737
738

Figure 2

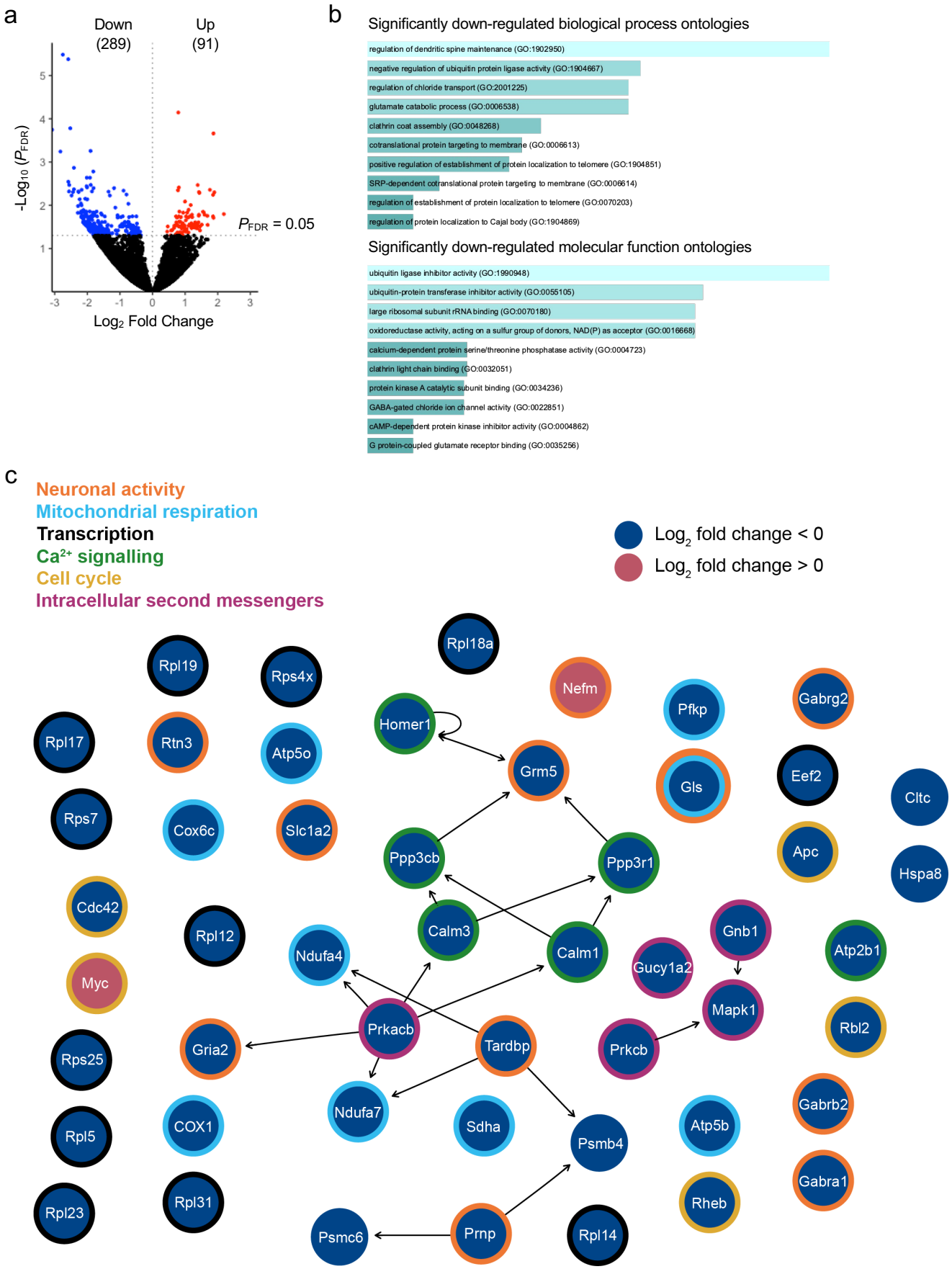
a
Down
(289)
Up
(91)
-Log10 (PFDR)
PFDR = 0.05
Log2 Fold Change
b
Significantly down-regulated biological process ontologies
regulation of dendritic spine maintenance (GO:1902950)
negative regulation of ubiquitin protein ligase activity (GO:1904667)
regulation of chloride transport (GO:2001225)
glutamate catabolic process (GO:0006538)
clathrin coat assembly (GO:0048268)
cotranslational protein targeting to membrane (GO:0006613)
positive regulation of establishment of protein localization to telomere (GO:1904851)
SRP-dependent cotranslational protein targeting to membrane (GO:0006614)
regulation of establishment of protein localization to telomere (GO:0070203)
regulation of protein localization to Cajal body (GO:1904869)
Significantly down-regulated molecular function ontologies
ubiquitin ligase inhibitor activity (GO:1990948)
ubiquitin-protein transferase inhibitor activity (GO:0055105)
large ribosomal subunit rRNA binding (GO:0070180)
oxidoreductase activity, acting on a sulfur group of donors, NAD(P) as acceptor (GO:0016668)
calcium-dependent protein serine/threonine phosphatase activity (GO:0004723)
clathrin light chain binding (GO:0032051)
protein kinase A catalytic subunit binding (GO:0034236)
GABA-gated chloride ion channel activity (GO:0022851)
cAMP-dependent protein kinase inhibitor activity (GO:0004862)
G protein-coupled glutamate receptor binding (GO:0035256)
c
Neuronal activity
Mitochondrial respiration
Transcription
Ca2+ signalling
Cell cycle
Intracellular second messengers
Log2 fold change < 0
Log2 fold change > 0
Rpl18a
Rpl19
Rps4x
Nefm
Pfkp
Gabrg2
Homer1
Rpl17
Rtn3
Atp5o
Grm5
Gls
Eef2
Cltc
Rps7
Cox6c
Slc1a2
Ppp3cb
Ppp3r1
Apc
Hspa8
Cdc42
Rpl12
Calm3
Calm1
Gnb1
Atp2b1
Ndufa4
Gucy1a2
Myc
Mapk1
Rbl2
Prkacb
Tardbp
Prkcb
Rps25
Gria2
Ndufa7
Gabrb2
Rpl5
COX1
Sdha
Psmb4
Atp5b
Gabra1
Rpl23
Rpl31
Rheb
Psmc6
Prnp
Rpl14

**Figure 3: pCS regulates cerebromicrovascular cell permeability *in vitro* through activation of the EGFR.** a) Stimulation of hCMEC/D3 cells with pCS (24 h, 10 μM) has no effect on cell surface expression of EGFR; data are mean ± s.e.m., n = 4 independent experiments; representative flow cytometry histograms are shown. b) Treatment of hCMEC/D3 cells with pCS (10 μM) causes a time-dependent increase in EGFR Tyr1068 phosphorylation, maintained for at least 30 min; data are mean ± s.e.m., n = 9 independent experiments; representative flow cytometry histograms are shown. c) Pre-treatment of hCMEC/D3 cells with erlotinib (2.5 μM, 10 min) prevents EGFR Tyr1068 phosphorylation in response to pCS treatment (10 μM, 30 min), data are mean ± s.e.m., n = 6 independent experiments; representative flow cytometry histograms are shown. d) Pre-treatment of hCMEC/D3 cell monolayers with erlotinib (2.5 μM, 10 min) prevents the increase in paracellular permeability to a 70 kDa FITC-dextran conjugate induced by pCS stimulation (10 μM, 24 h); data are mean ± s.e.m., n = 9 independent experiments. e) Pre-treatment of hCMEC/D3 cell monolayers with erlotinib (2.5 μM, 10 min) prevents the reduction in TEER induced by pCS stimulation (10 μM, 24 h); data are mean ± s.e.m., n = 9 independent experiments. f) Confocal microscopic analysis of expression of the tight junction component zona occludens-1 (ZO-1; white) in hCMEC/D3 cells following treatment with either pCS (10 μM, 24 h), erlotinib (2.5 μM, 24 h) or both (erlotinib 2.5 μM, 10 min pre-treatment, followed by pCS 10 μM, 24 h); nuclei are counterstained with DAPI (blue), scale bar = 15 μm. Images are representative of at least three independent experiments. g) Confocal microscopic analysis of expression of AF488-conjugated phalloidin labelled actin filaments (white) in hCMEC/D3 cells following treatment with either pCS (10 μM, 24 h), erlotinib (2.5 μM, 24 h) or both (erlotinib 2.5 μM, 10 min pre-treatment, followed by pCS 10 μM, 24 h); nuclei are counterstained with DAPI (blue), scale bar = 15 μm. Images are representative of at least three independent experiments. h) Paracellular permeability to a 70 kDa FITC-dextran conjugate of hCMEC/D3 cell monolayers bearing siRNA sequences targeting the EGFR (siRNA 5, siRNA 11, siRNA 12), a non-targeting negative control siRNA sequence, or that had been mock transfected, with or without stimulation with pCS (10 μM, 24 h); data are mean ± s.e.m., n = 4 independent experiments. i) TEER of hCMEC/D3 cell monolayers bearing siRNA sequences targeting the EGFR (siRNA 5, siRNA 11, siRNA 12), a non-targeting negative control siRNA sequence, or that had been mock transfected, with or without stimulation with pCS (10 μM, 24 h); data are mean ± s.e.m., n = 3 independent experiments.

Figure 3

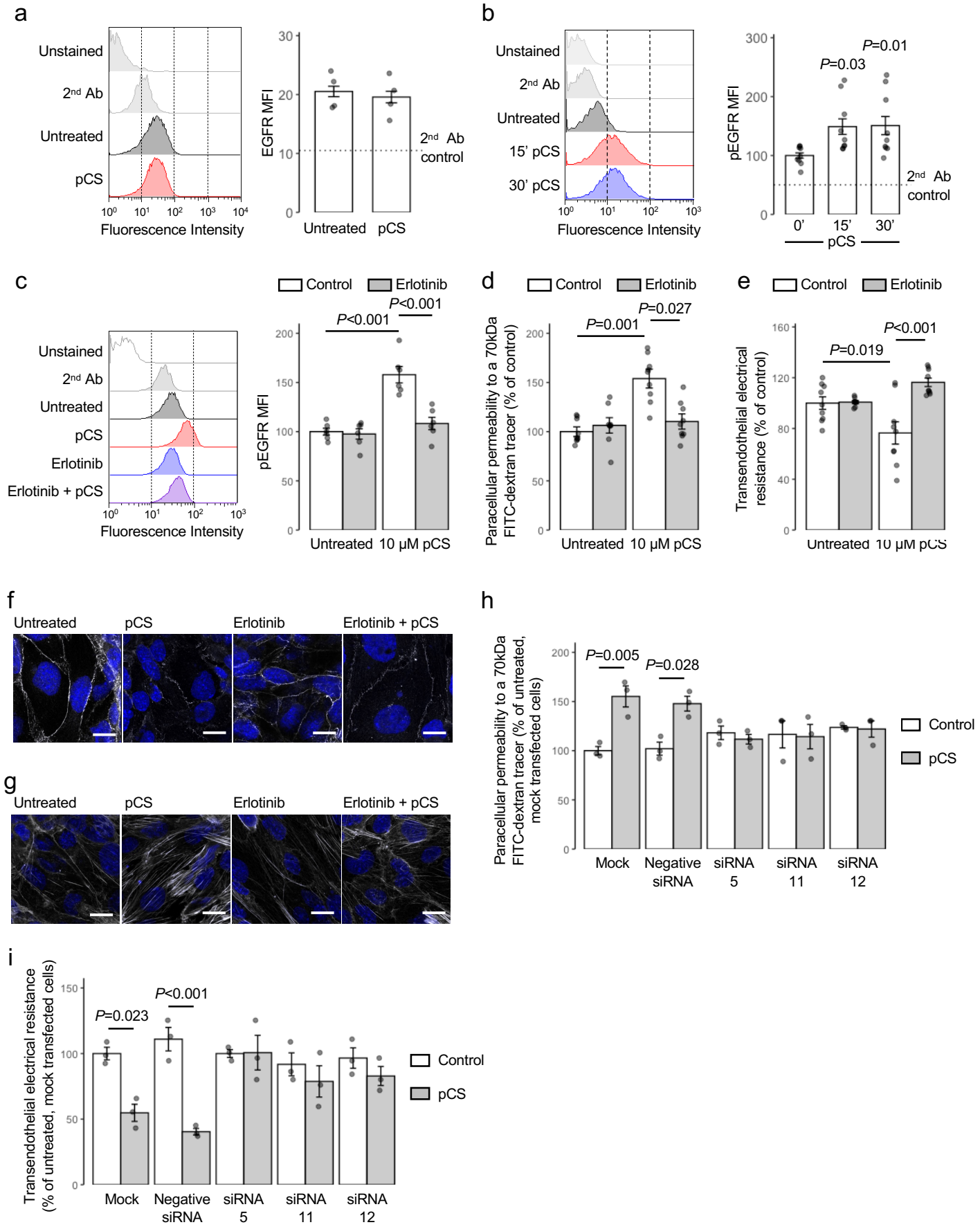
a
Unstained
2nd Ab
Untreated
pCS
Fluorescence Intensity
EGFR MFI
2nd Ab control
Untreated
pCS
b
Unstained
2nd Ab
Untreated
15' pCS
30' pCS
Fluorescence Intensity
pEGFR MFI
P=0.01
P=0.03
2nd Ab control
0'
15'
30'
pCS
c
Control
Erlotinib
Unstained
2nd Ab
Untreated
pCS
Erlotinib
Erlotinib + pCS
Fluorescence Intensity
pEGFR MFI
P<0.001
P<0.001
Untreated
10 μM pCS
d
Control
Erlotinib
Paracellular permeability to a 70kDa FITC-dextran tracer (% of control)
P=0.001
P=0.027
Untreated
10 μM pCS
e
Control
Erlotinib
Transendothelial electrical resistance (% of control)
P=0.019
P<0.001
Untreated
10 μM pCS
f
Untreated
pCS
Erlotinib
Erlotinib + pCS
g
Untreated
pCS
Erlotinib
Erlotinib + pCS
h
Paracellular permeability to a 70kDa FITC-dextran tracer (% of untreated, mock transfected cells)
P=0.005
P=0.028
Control
pCS
Mock
Negative siRNA
siRNA 5
siRNA 11
siRNA 12
i
Transendothelial electrical resistance (% of untreated, mock transfected cells)
P=0.023
P<0.001
Control
pCS
Mock
Negative siRNA
siRNA 5
siRNA 11
siRNA 12

773 **Figure 4: Stimulation of EGFR by pCS activates a downstream ANXA1–STAT3**
774 **signalling pathway.** a) Stimulation of hCMEC/D3 cells with pCS (10 μM, 30 min) increases
775 the ratio of Tyr21 phosphorylated to total annexin A1; data are mean ± s.e.m., n = 7
776 independent experiments; representative flow cytometry histograms are shown. b) Pre-
777 treatment of hCMEC/D3 cells with erlotinib (2.5 μM, 10 min) prevents the increase in the Tyr21
778 phosphorylated to total ANXA1 expression ratio induced by pCS stimulation (10 μM, 30 min);
779 data are mean ± s.e.m., n = 6 independent experiments. c) Paracellular permeability to a 70
780 kDa FITC-dextran tracer of monolayers of wild-type hCMEC/D3 cells, or hCMEC/D3 cells
781 stably transfected with either a scramble shRNA sequence or one of three independent shRNA
782 sequences targeting ANXA1 following stimulation with pCS (10 μM, 24 h); data are mean ±
783 s.e.m., *n* = 4 independent experiments. d) TEER of monolayers of wild-type hCMEC/D3 cells,
784 or hCMEC/D3 cells stably transfected with either a scramble shRNA sequence or one of three
785 independent shRNA sequences targeting ANXA1 following stimulation with pCS (10 μM, 24
786 h); data are mean ± s.e.m., *n* = 4 independent experiments. e) Stimulation of hCMEC/D3 cells
787 with pCS (10 μM) causes a time-dependent increase in expression of Tyr705 phosphorylated
788 STAT3; data are mean ± s.e.m., n = 7 independent experiments; representative flow cytometry
789 histograms are shown. f) Pre-treatment of hCMEC/D3 cells with erlotinib (2.5 μM, 10 min)
790 prevents the increase in Tyr705 phosphorylated STAT3 expression induced by pCS treatment
791 (10 μM, 30 min); data are mean ± s.e.m., n = 6 independent experiments. g) Expression of
792 Tyr705 phosphorylated STAT3 in wild-type hCMEC/D3 cells, or hCMEC/D3 cells stably
793 transfected with either a scramble shRNA sequence or one of three independent shRNA
794 sequences targeting ANXA1 following stimulation with pCS (10 μM), expressed as percentage
795 of untreated cells; data are mean ± s.e.m., n = 4 independent experiments. h) Pre-treatment
796 of hCMEC/D3 cell monolayers with the STAT3 inhibitor C188-9 (5 μM, 30 min) prevents the
797 increase in paracellular permeability to a 70 kDa FITC-dextran conjugate induced by pCS
798 stimulation (10 μM, 24 h); data are mean ± s.e.m., n = 6 independent experiments. i) Pre-
799 treatment of hCMEC/D3 cell monolayers with C188-9 (5 μM, 30 min) prevents the reduction
800 in TEER induced by pCS stimulation (10 μM, 24 h); data are mean ± s.e.m., n = 6 independent
801 experiments.
802
803

Figure 4

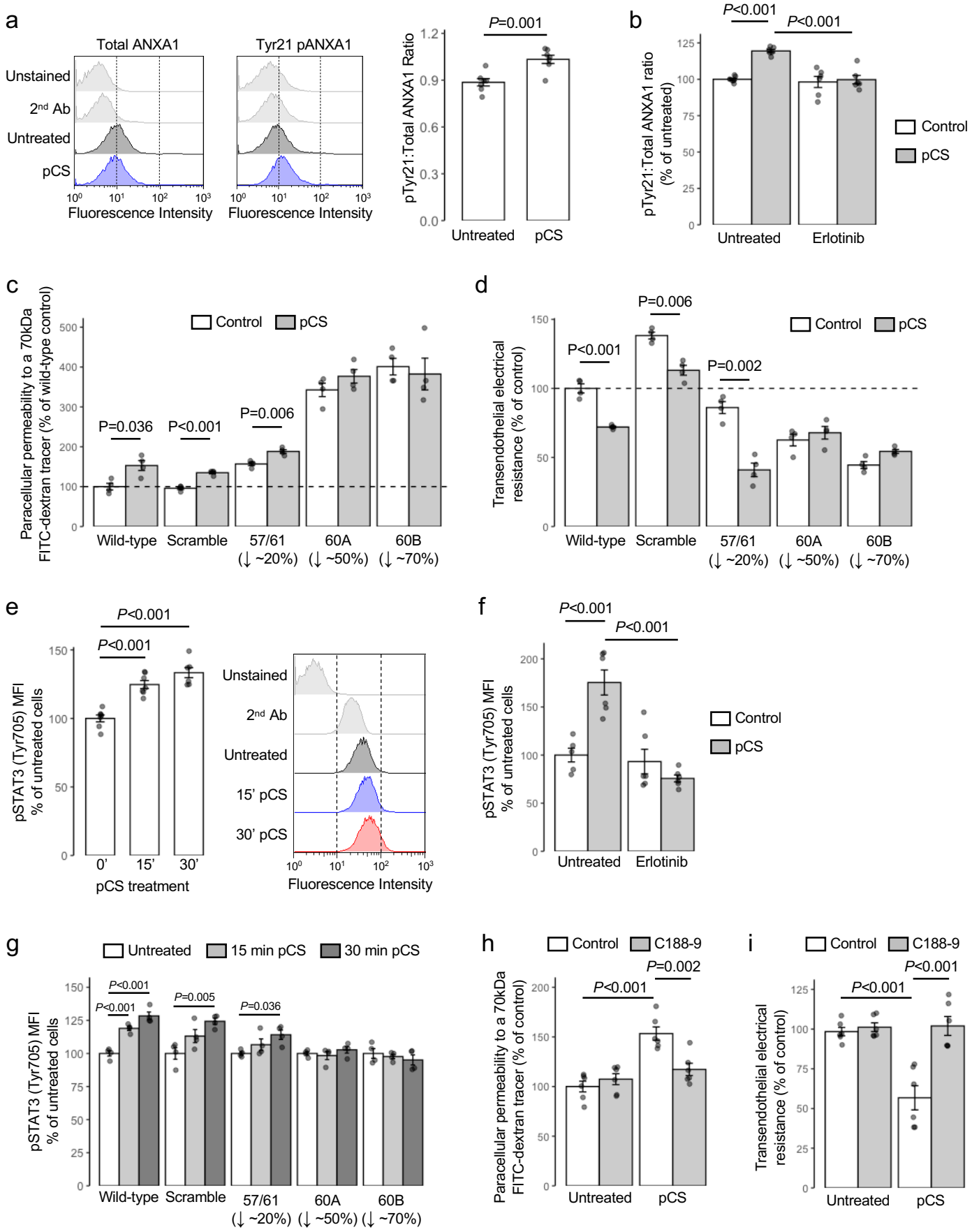
a
Total ANXA1
Tyr21 pANXA1
Unstained
2nd Ab
Untreated
pCS
Fluorescence Intensity
pTyr21:Total ANXA1 Ratio
P=0.001
Untreated
pCS
b
P<0.001
P<0.001
pTyr21:Total ANXA1 ratio (% of untreated)
Control
pCS
Untreated
Erlotinib
c
Paracellular permeability to a 70kDa FITC-dextran tracer (% of wild-type control)
Control
pCS
P=0.036
P<0.001
P=0.006
Wild-type
Scramble
57/61 (↓ ~20%)
60A (↓ ~50%)
60B (↓ ~70%)
d
Transendothelial electrical resistance (% of control)
P=0.006
P<0.001
P=0.002
e
P<0.001
P<0.001
pSTAT3 (Tyr705) MFI % of untreated cells
0'
15'
30'
pCS treatment
Unstained
2nd Ab
Untreated
15' pCS
30' pCS
Fluorescence Intensity
f
P<0.001
P<0.001
Untreated
Erlotinib
g
Untreated
15 min pCS
30 min pCS
P<0.001
P<0.001
P=0.005
P=0.036
h
Control
C188-9
P=0.002
P<0.001
i
P<0.001
P<0.001

**Figure 5: pCS enhances endothelial permeability *via* mobilisation of active MMP2 and MMP9.** a) Treatment of hCMEC/D3 cells with pCS (10 μM, 24 h) increases expression of MMP2 and MMP9; data are mean ± s.e.m., n = 7 independent experiments. b) Stimulation of MMP2 or MMP9 expression in hCMEC/D3 cells by pCS (10 μM, 24 h) is prevented by either erlotinib (2.5 μM, 10 min pre-treatment) or C188-9 (5 μM, 30 min pre-treatment); data are mean ± s.e.m., n = 6 independent experiments. c) Active MMP2 and MMP9 are secreted into the culture medium of hCMEC/D3 cells in response to pCS (10 μM, 24 h) stimulation; data are mean ± s.e.m., n = 6 independent experiments; a typical gelatin zymography is shown, highlighting both active MMP2 and MMP9 and artifactually revealed pro-MMP2 and pro-MMP9 activity. d) Active MMP2 and MMP9 release from hCMEC/D3 cells into culture medium in response to pCS (10 μM, 24 h) stimulation is prevented by erlotinib (2.5 μM, 10 min pre-treatment); data are mean ± s.e.m., n = 11-12 independent replicates. e) Pre-treatment of hCMEC/D3 cell monolayers with the MMP2 inhibitor ARP 100 (12 nM, 15 min) prevents the increase in paracellular permeability to a 70 kDa FITC-dextran conjugate induced by pCS stimulation (10 μM, 24 h); data are mean ± s.e.m., n = 6 independent experiments. f) Pre-treatment of hCMEC/D3 cell monolayers with ARP 100 (12 nM, 15 min) prevents the reduction in TEER induced by pCS stimulation (10 μM, 24 h); data are mean ± s.e.m., n = 6 independent experiments. g) Confocal microscopic analysis of expression of the tight junction component zona occludens-1 (ZO-1; white) in hCMEC/D3 cells following treatment with either pCS (10 μM, 24 h), ARP 100 (12 nM, 24 h) or both (ARP 100 12 nM, 15 min pre-treatment, followed by pCS 10 μM, 24 h); nuclei are counterstained with DAPI (blue), scale = 15 μm . Images are representative of at least three independent experiments. h) Pre-treatment of hCMEC/D3 cell monolayers with the MMP9 inhibitor JNJ0966 (440 nM, 15 min) prevents the increase in paracellular permeability to a 70 kDa FITC-dextran conjugate induced by pCS stimulation (10 μM, 24 h); data are mean ± s.e.m., n = 6 independent experiments. i) Pre-treatment of hCMEC/D3 cell monolayers with JNJ0966 (440 nM, 15 min) prevents the reduction in TEER induced by pCS stimulation (10 μM, 24 h); data are mean ± s.e.m., n = 6 independent experiments. j) Confocal microscopic analysis of expression of the tight junction component zona occludens-1 (ZO-1; white) in hCMEC/D3 cells following treatment with either pCS (10 μM, 24 h), JNJ0966 (440 nM, 24 h) or both (JNJ0966 440 nM, 15 min pre-treatment, followed by pCS 10 μM, 24 h); nuclei are counterstained with DAPI (blue), scale = 15 μm. Images are representative of at least three independent experiments.

Figure 5

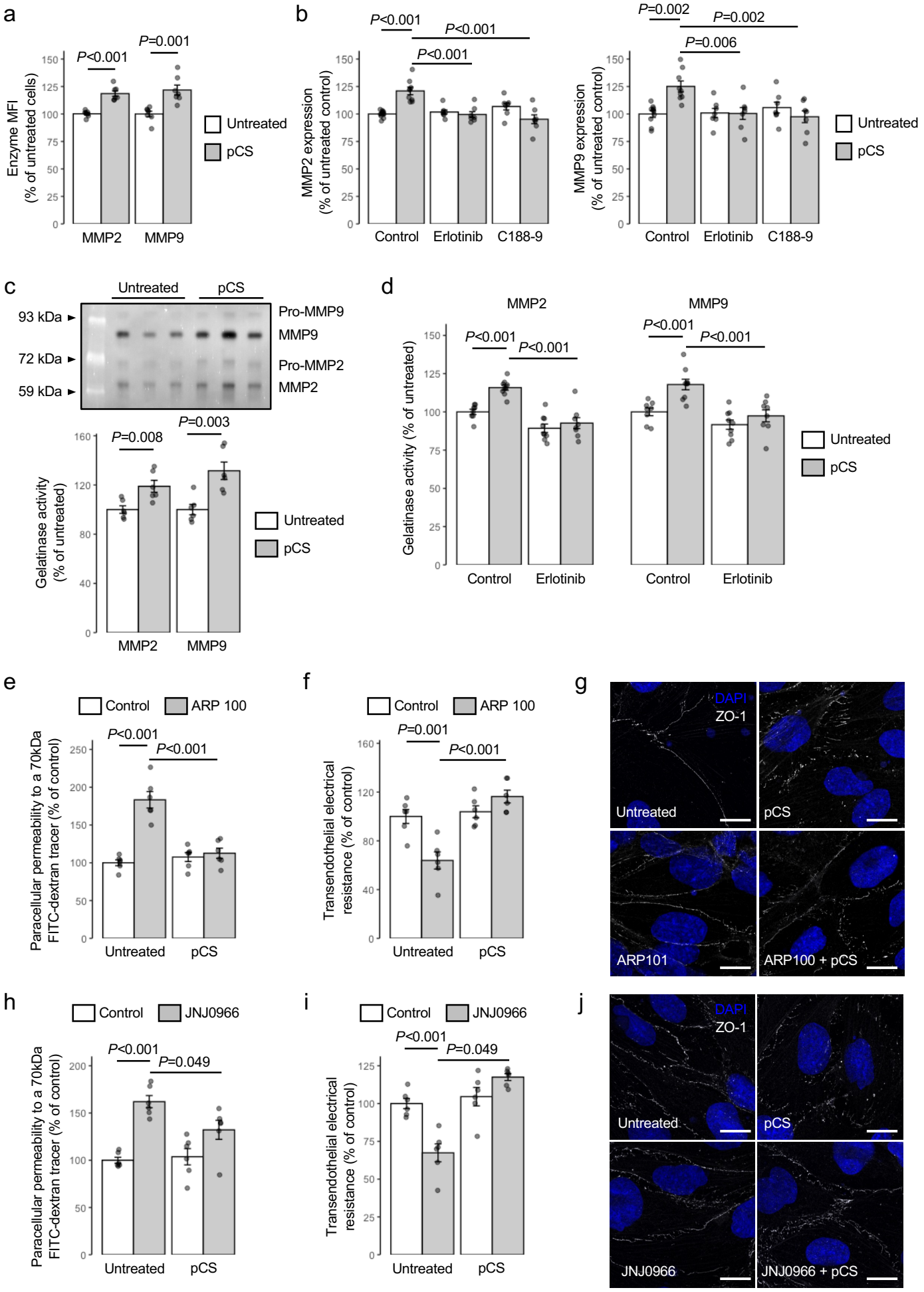
a
Enzyme MFI (% of untreated cells)
P<0.001
P=0.001
MMP2
MMP9
Untreated
pCS
b
MMP2 expression (% of untreated control)
P<0.001
P<0.001
P<0.001
Control
Erlotinib
C188-9
MMP9 expression (% of untreated control)
P=0.002
P=0.002
P=0.006
c
Untreated
pCS
93 kDa
72 kDa
59 kDa
Pro-MMP9
MMP9
Pro-MMP2
MMP2
Gelatinase activity (% of untreated)
P=0.008
P=0.003
d
MMP2
MMP9
P<0.001
P<0.001
e
Control
ARP 100
Paracellular permeability to a 70kDa FITC-dextran tracer (% of control)
f
Transendothelial electrical resistance (% of control)
P=0.001
g
DAPI
ZO-1
Untreated
pCS
ARP101
ARP100 + pCS
h
JNJ0966
P=0.049
i
j
JNJ0966
JNJ0966 + pCS

838 **Figure 6: Treatment with pCS induces BBB permeability *in vivo* through EGFR-**
839 **dependent mobilisation of MMP9.** a, b) Confocal microscopic analysis of expression of a)
840 MMP-2 or b) MMP-9 (magenta) in the brains of male C57Bl/6 exposed to pCS by s.c.
841 implantation with osmotic mini-pumps releasing at 7.5 µg/h for 28 days, blood vessels are
842 defined by tomato lectin binding (cyan), nuclei are counterstained with DAPI (white), scale =
843 10 µm, images are representative of 7-10 animals. c, d) Confocal microscopic analysis of c)
844 MMP2 and d) MMP9 expression (magenta) within the cerebral microvasculature of male
845 C57Bl/6 mice exposed to pCS (10 mg/kg, i.p. 2 h) with or without erlotinib pre-treatment (50
846 mg/kg, i.p. 1 h pre-treatment); blood vessels are defined by tomato lectin binding (cyan), nuclei
847 are counterstained with DAPI (white), scale bar = 5 µm, images are representative of 7-10
848 animals. e) Typical expression of ZO-1 (white) within the cerebral microvasculature of male
849 C57Bl/6 mice exposed to pCS (10 mg/kg, i.p. 2 h) with or without erlotinib pre-treatment (50
850 mg/kg, i.p. 1 h pre-treatment); nuclei are counterstained with DAPI (blue), scale bar = 10 µm.
851 Typical expression of ZO-1 (white) within the cerebral microvasculature of male C57Bl/6 mice
852 exposed to pCS (10 mg/kg, i.p. 2 h) with or without erlotinib pre-treatment (50 mg/kg, i.p. 1 h
853 pre-treatment); nuclei are counterstained with DAPI (blue), scale bar = 10 µm. f) Increased
854 extravasation of Evans blue tracer into the parenchyma of male C57Bl/6 mice following i.p.
855 injection of pCS (10 mg/kg, 2 h exposure) is prevented by erlotinib administration (50 mg/kg
856 i.p., 1 h pre-treatment); data are mean ± s.e.m., n = 5-6 animals. g) Increased extravasation
857 of Evans blue tracer into the parenchyma of male C57Bl/6 mice following i.p. injection of pCS
858 (10 mg/kg, 2 h exposure) is prevented by administration of the dual-specific MMP2/MMP9
859 inhibitor SB-3CT (10 mg/kg i.p., 1 h pre-treatment); data are mean ± s.e.m., n = 5-6 animals.
860
861

Figure 6

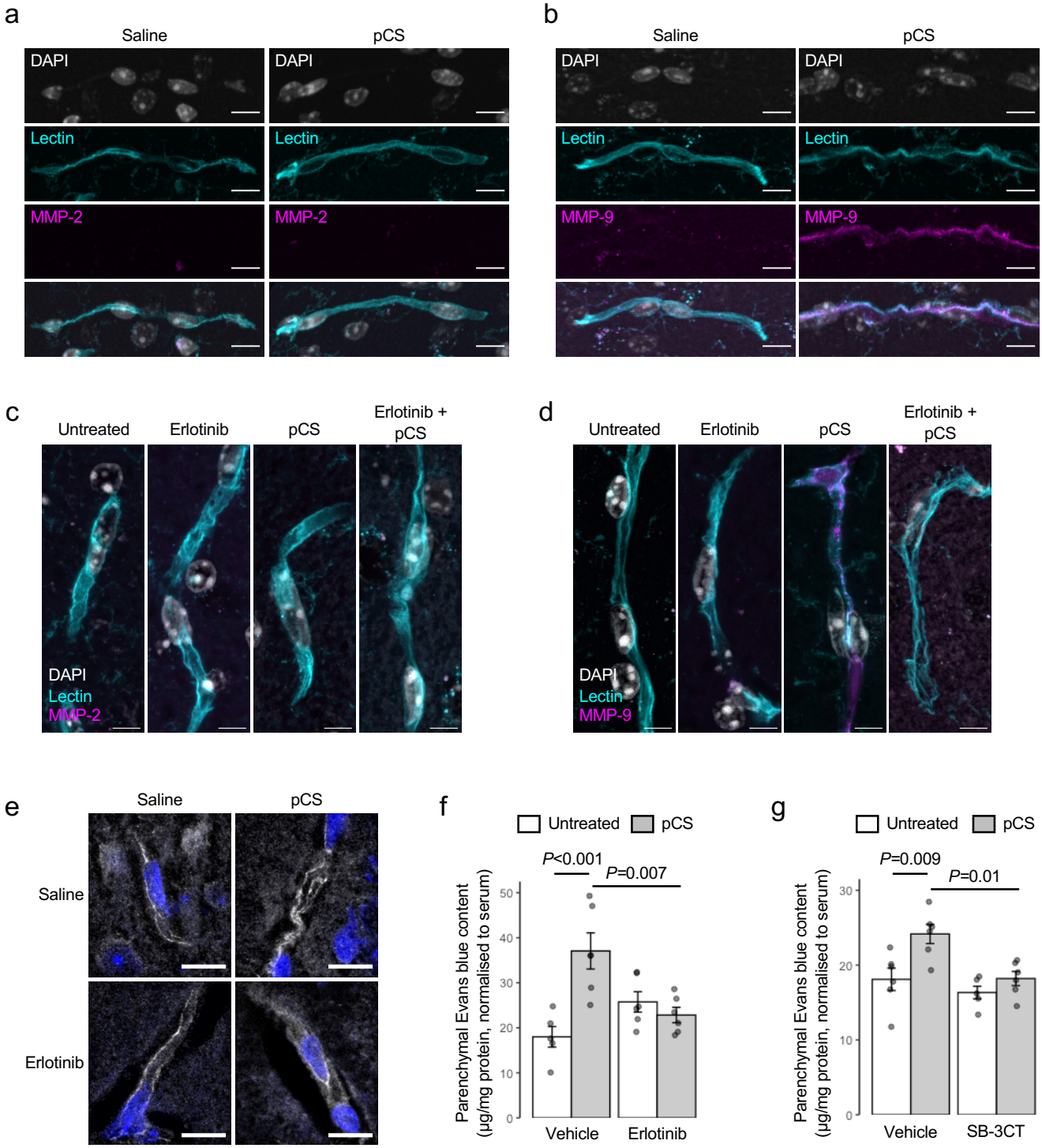
a
Saline
pCS
DAPI
Lectin
MMP-2
b
Saline
pCS
DAPI
Lectin
MMP-9
c
Untreated
Erlotinib
pCS
Erlotinib + pCS
DAPI
Lectin
MMP-2
d
Untreated
Erlotinib
pCS
Erlotinib + pCS
DAPI
Lectin
MMP-9
e
Saline
pCS
Saline
Erlotinib
f
Untreated
pCS
P<0.001
P=0.007
Parenchymal Evans blue content (µg/mg protein, normalised to serum)
0
10
20
30
40
50
Vehicle
Erlotinib
g
Untreated
pCS
P=0.009
P=0.01
Parenchymal Evans blue content (µg/mg protein, normalised to serum)
0
10
20
30
Vehicle
SB-3CT

862 **Figure 7: Sera from human haemodialysis patients significantly enhances endothelial**
863 **permeability, an effect prevented by erlotinib pre-treatment.** a) Treatment of hCMEC/D3
864 monolayers with medium containing de-complemented sera from patients undergoing
865 haemodialysis (20 %, 24 h) significantly enhances permeability to a 70 kDa FITC-dextran
866 tracer, an effect not seen with equivalent sera from healthy donors, and prevented by inclusion
867 of erlotinib (2.5 μM, 10 min); data are mean ± s.e.m., n = 10-11 donors. b) TEER of hCMEC/D3
868 monolayers is not affected by treatment with media containing sera (20 %, 24 h) from either
869 haemodialysis patients or healthy donors, nor by erlotinib inclusion (2.5 μM, 10 min pre-
870 treatment); data are mean ± s.e.m., n = 10-11 donors. c) Treatment of hCMEC/D3 cells with
871 medium containing de-complemented sera (20 %, 24 h) from patients undergoing
872 haemodialysis, but not with that from healthy donors, increases expression of MMP2; data are
873 mean ± s.e.m., n = 10-11 donors. d) Treatment of hCMEC/D3 cells with medium containing
874 de-complemented sera (20 %, 24 h) from patients undergoing haemodialysis, but not with that
875 from healthy donors, increases expression of MMP9; data are mean ± s.e.m., n = 10-11
876 donors. e) Correlation between concentrations of pCS in human sera samples (healthy donors
877 in black, haemodialysis patients in red) with 70 kDa FITC-dextran permeability data from (a)
878 above; n = 10-11 donors. f) Correlation between concentrations of xanthurenic acid in human
879 sera samples (healthy donors in black, haemodialysis patients in red) with 70 kDa FITC-
880 dextran permeability data from (a) above; n = 10-11 donors.
881

Figure 7

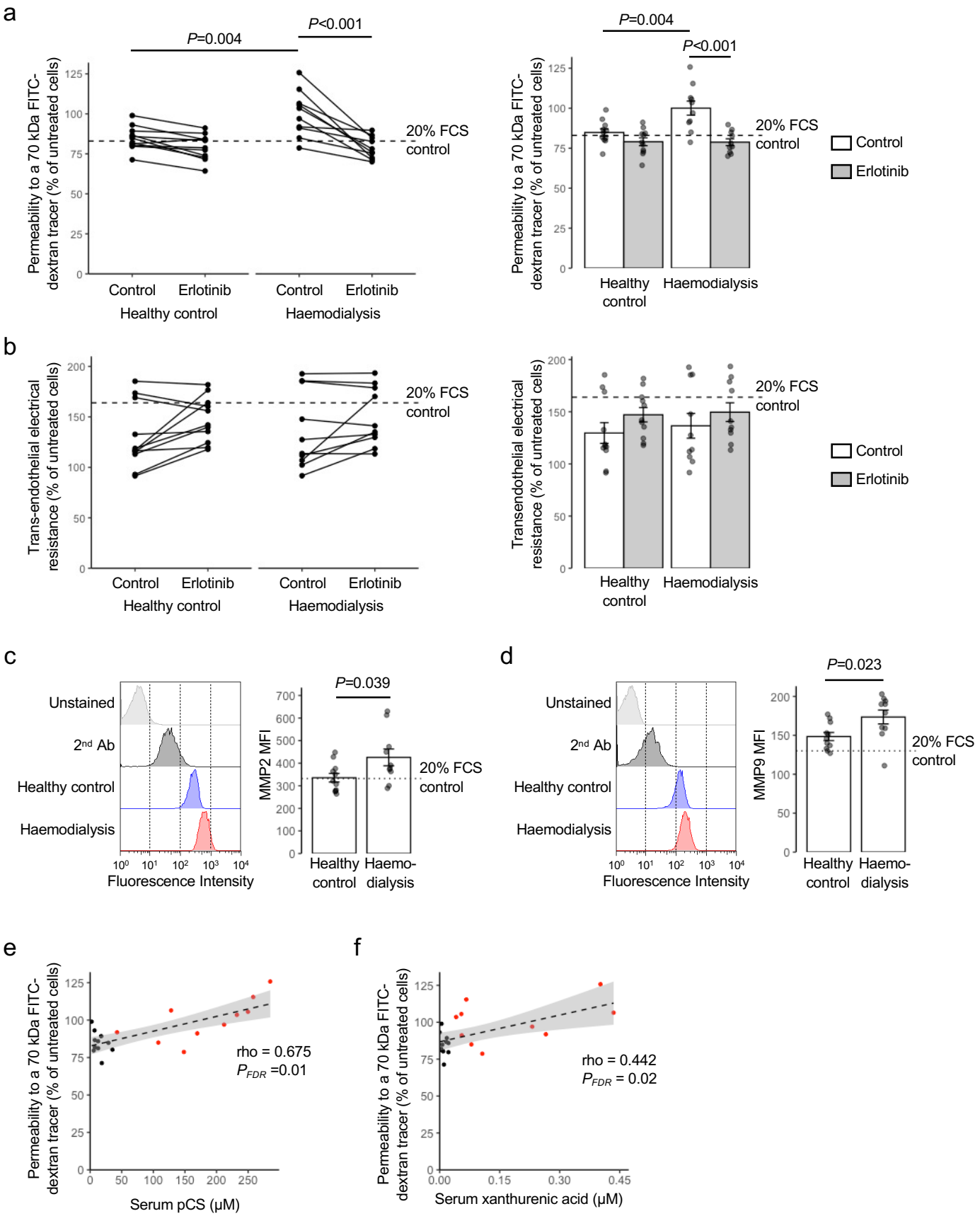
a
P=0.004
P<0.001
Permeability to a 70 kDa FITC-dextran tracer (% of untreated cells)
20% FCS control
Control
Erlotinib
Healthy control
Haemodialysis
b
Trans-endothelial electrical resistance (% of untreated cells)
Transendothelial electrical resistance (% of untreated cells)
c
Unstained
2nd Ab
Healthy control
Haemodialysis
Fluorescence Intensity
MMP2 MFI
Healthy control
Haemo-dialysis
d
MMP9 MFI
e
rho = 0.675
PFDR =0.01
Serum pCS (μM)
f
rho = 0.442
PFDR = 0.02
Serum xanthurenic acid (μM)

882 **Tables**

883

884 **Table 1: Significant results generated from SPIA of 380 significantly differentially**
885 **expressed genes.**

886

| Name | KEGG pathway ID | pGFdr | pGFWER | Status |
|---|---|---|---|---|
| Glutamatergic synapse | mmu:04724 | $2.83 \times 10^{-4}$ | $2.83 \times 10^{-4}$ | Inhibited |
| Circadian entrainment | mmu:04713 | $2.98 \times 10^{-3}$ | $5.97 \times 10^{-3}$ | Inhibited |
| Alzheimer disease | mmu:05010 | $1.40 \times 10^{-2}$ | $4.20 \times 10^{-2}$ | Inhibited |
| Amphetamine addiction | mmu:05031 | $1.92 \times 10^{-2}$ | $7.68 \times 10^{-2}$ | Inhibited |
| Oxytocin signalling pathway | mmu:04921 | $2.54 \times 10^{-2}$ | $1.27 \times 10^{-1}$ | Inhibited |
| Glucagon Signaling pathway | mmu:04922 | $2.75 \times 10^{-2}$ | $1.72 \times 10^{-1}$ | Inhibited |
| Retrograde endocannabinoid signalling | mmu:04723 | $2.75 \times 10^{-2}$ | $1.92 \times 10^{-1}$ | Inhibited |
| Pathways of neurodegeneration - multiple diseases | mmu:05022 | $2.98 \times 10^{-2}$ | $2.66 \times 10^{-1}$ | Inhibited |
| VEGF signalling pathway | mmu:04370 | $2.98 \times 10^{-2}$ | $2.68 \times 10^{-1}$ | Inhibited |
| Cellular senescence | mmu:04218 | $3.12 \times 10^{-2}$ | $3.13 \times 10^{-1}$ | Inhibited |
| Aldosterone synthesis and secretion | mmu:04925 | $3.12 \times 10^{-2}$ | $3.43 \times 10^{-1}$ | Inhibited |
| Ras signalling pathway | mmu:04014 | $4.14 \times 10^{-2}$ | $4.96 \times 10^{-1}$ | Inhibited |
| C-type lectin receptor signalling pathway | mmu:04625 | $4.18 \times 10^{-2}$ | $5.44 \times 10^{-1}$ | Inhibited |
| Coronavirus disease - COVID-19 | mmu:05171 | $4.59 \times 10^{-2}$ | $6.42 \times 10^{-1}$ | Activated |
| Lipid and atherosclerosis | mmu:05417 | $4.83 \times 10^{-2}$ | $7.24 \times 10^{-1}$ | Inhibited |
| Gastric acid secretion | mmu:04971 | $4.94 \times 10^{-2}$ | $7.90 \times 10^{-1}$ | Inhibited |
| Huntington disease | mmu:05016 | $4.97 \times 10^{-2}$ | $8.45 \times 10^{-1}$ | Inhibited |

887

888

889 **Table 2: Serum donor demographics.**

890

| | Age (years) | Sex ratio | Serum urea (mg/dl) | Serum creatinine (μM) | Renal replacement therapy duration (years) |
|---|---|---|---|---|---|
| **Healthy donor** | 49 ± 3.3 | 8F : 3M | 4.46 ± 0.36 | 82.0 ± 6.8 | N/A |
| **Haemodialysis** | 59 ± 6.2 | 4F : 6M | 19.13 ± 1.90 | 876.2 ± 94.7 | 10.6 ± 4.2 |

891

892 **Table 3: Human haemodialysis patient serum metabolite concentrations.** LC-MS/MS
893 determined concentrations of different potential uraemic toxins in sera from healthy donors
894 and individuals undergoing haemodialysis for nephropathy, alongside coefficients of
895 correlation between metabolite concentration and permeability of hCMEC/D3 cells to a 70 kDa
896 FITC-dextran tracer following treatment with 20% sera for 24 h; n = 10-11, * $P<0.05$ *vs.* healthy
897 donors.
898

| **Metabolite** | **Healthy donor (μM)** | **Haemodialysis (μM)** | **Permeability correlation** | |
|---|---|---|---|---|
| | | | **Rho** | $P_{FDR}$ |
| *p*-Cresol sulfate | 14.12 ± 3.09 | 155.26 ± 27.36 * | 0.675 | 0.01 |
| *p*-Cresol glucuronide | 0.09 ± 0.03 | 10.63 ± 4.44 * | 0.394 | 0.12 |
| Indoxyl sulfate | 2.92 ± 0.45 | 147.18 ± 26.46 * | 0.400 | 0.09 |
| Serotonin | 0.64 ± 0.12 | 0.42 ± 0.18 | -0.233 | 0.64 |
| Kynurenine | 1.73 ± 0.23 | 4.63 ± 0.57 * | 0.371 | 0.06 |
| 3-Hydroxyanthranilic acid | 0.01 ± 0.00 | 0.05 ± 0.01 * | 0.434 | 0.11 |
| Tryptophan | 42.30 ± 1.46 | 22.97 ± 2.35 * | -0.466 | 0.06 |
| 5-Hydroxyindole acetic acid | 0.05 ± 0.01 | 1.28 ± 0.21 * | 0.464 | 0.08 |
| Xanthurenic acid | 0.01 ± 0.00 | 0.17 ± 0.05 * | 0.442 | 0.02 |
| Anthranilic acid | 0.20 ± 0.02 | 0.52 ± 0.1 * | 0.396 | 0.12 |
| Kynurenic acid | 0.06 ± 0.01 | 2.34 ± 0.58 * | 0.353 | 0.16 |
| Indole-3-lactic acid | 0.78 ± 0.12 | 2.42 ± 0.33 * | 0.397 | 0.12 |
| Indole-3-carboxaldehyde | 0.05 ± 0.00 | 0.06 ± 0.01 | -0.08 | 0.78 |
| Indole-carboxylic acid | 0.04 ± 0.01 | 0.06 ± 0.01 | 0.041 | 0.89 |
| Indole-3-acetic acid | 2.45 ± 0.75 | 6.36 ± 2.07 | 0.385 | 0.17 |
| Indole-3-propionic acid | 1.73 ± 0.4 | 1.37 ± 0.35 | 0.051 | 0.47 |
| Methyl indole 3-acetate | 0.05 ± 0.03 | 7.44 ± 3.48 * | 0.241 | 0.43 |

899

**Extended Data**

Figure 1: Confirmation of specificity of pCS effects upon endothelial barrier function in hCMEC/D3 cells.

Figure 2: Treatment of hCMEC/D3 cells with albumin prevented the effects of pCS upon endothelial barrier function.

Figure 3: Mice exposed to raised levels of pCS for 4 weeks do not show any obvious changes in cortical microglial or astrocyte morphology or density.

Figure 4: Mice exposed to raised levels of pCS for 4 weeks do not show overt behavioural changes on the open field test, Y-maze or novel object recognition task.

Figure 5: Confirmation of RNA interference knock-down experiments.

Figure 6: *In vivo* administration of pCS stimulates Tyr21 phosphorylation of ANXA1 in an erlotinib-sensitive manner.

Figure 7: Treatment of hCMEC/D3 cells with indoxyl sulfate (IS) does not affect endothelial barrier functions at physiological or uraemia-associated concentrations.

Table 1: Circulating concentrations (μM) of tryptophan and p-cresol metabolites in mice exposed for 8 weeks to pCS or saline *via* osmotic minipumps.

Table 2: Outputs from DESeq2 analysis of differentially expressed genes.

Table 3: Summary network statistics for transcriptomic data mapped to KEGG pathways.

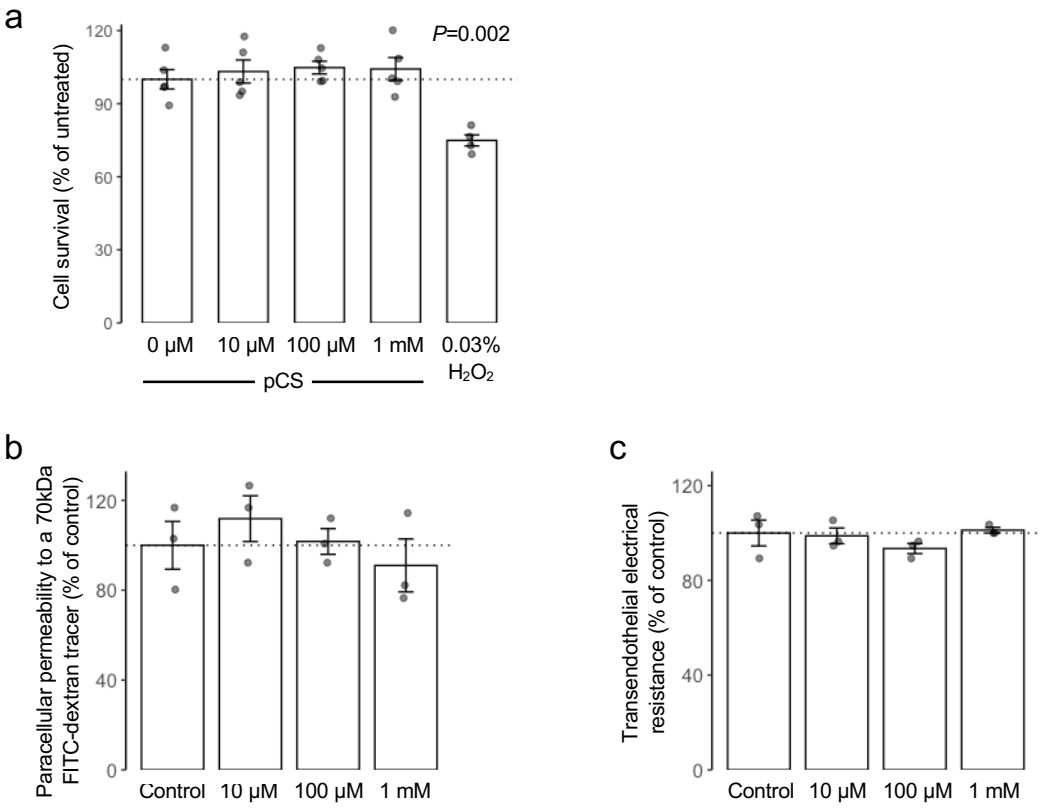


**Extended Data Figure 1: Confirmation of specificity of pCS effects upon endothelial barrier function in hCMEC/D3 cells.** a) Treatment of hCMEC/D3 cells with increasing concentrations of pCS (10 µM, 100 µM, 1 mM, 24 h) does not affect cell viability as assessed by MTT assay, in contrast to treatment with 0.03 % $H_2O_2$ (24 h), which caused a significant loss in viability; data are mean ± s.e.m., n = 5 independent experiments. b) Incubation of hCMEC/D3 cell monolayers with KCl (10 µM - 1 mM; 24 h) did not significantly affect paracellular permeability to a 70 kDa FITC-dextran conjugate; data are mean ± s.e.m., n = 3 independent experiments. c) Incubation of hCMEC/D3 cell monolayers with KCl (10 µM - 1 mM; 24 h) did not significantly affect TEER; data are mean ± s.e.m., n = 3 independent experiments.

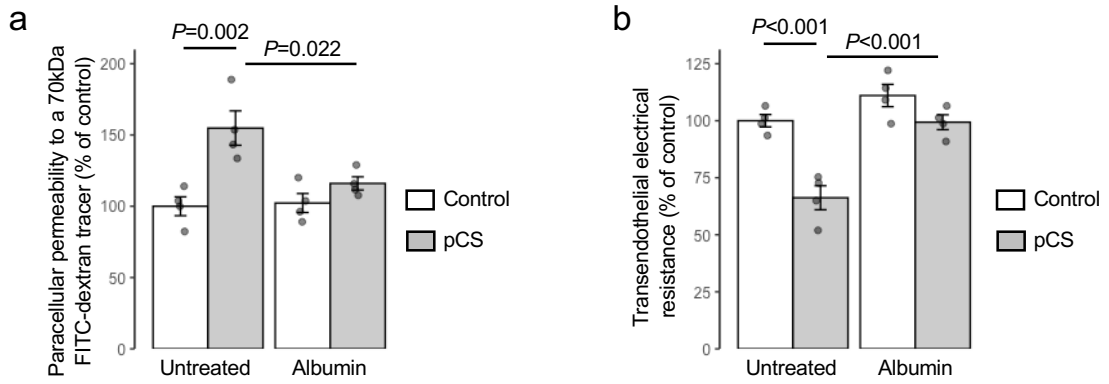


**Extended Data Figure 2: Treatment of hCMEC/D3 cells with albumin prevented the effects of pCS upon endothelial barrier function.** a) Incubation of hCMEC/D3 cell monolayers with human albumin (50 mg/ml) in conjunction with pCS (10 μM, 24 h) prevented the effects of pCS upon paracellular permeability to a 70 kDa FITC-dextran conjugate; data are mean ± s.e.m., n = 4 independent experiments. b) Incubation of hCMEC/D3 cell monolayers with human albumin (50 mg/ml) in conjunction with pCS (10 μM, 24 h) prevented the effects of pCS upon trans-endothelial electrical resistance; data are mean ± s.e.m., n = 4 independent experiments.

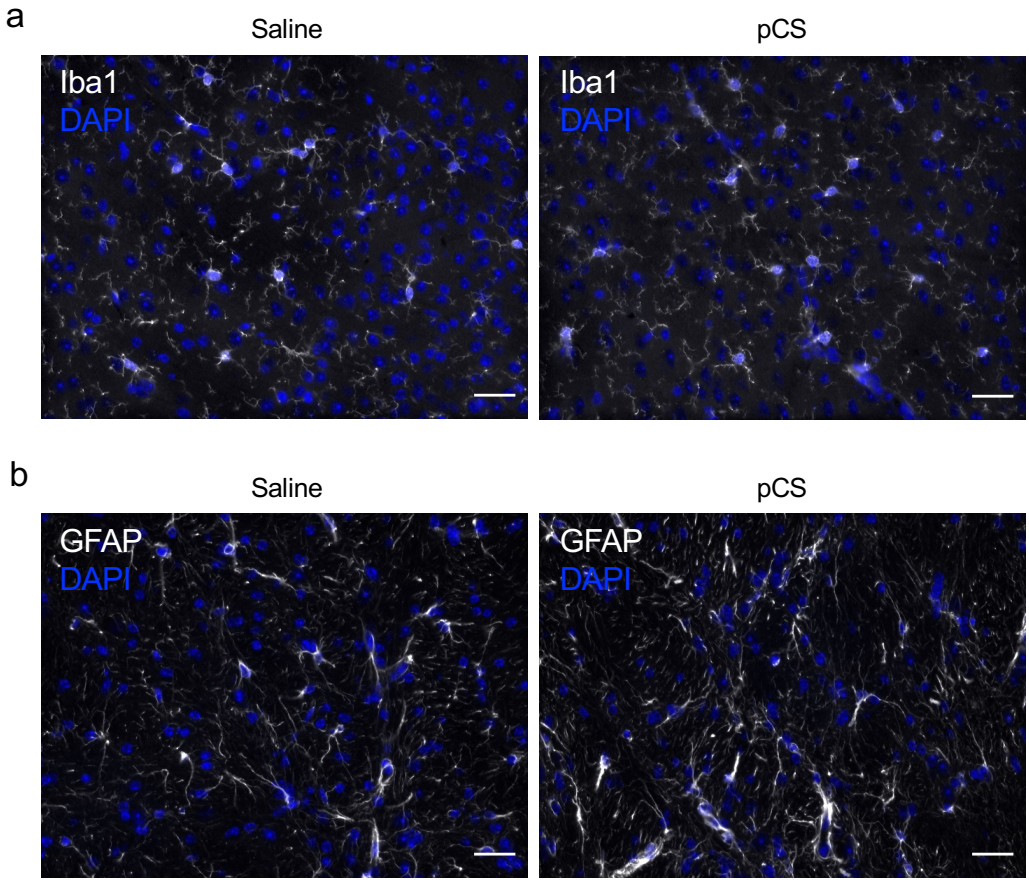


**Extended Data Figure 3: Mice exposed to raised levels of pCS for 4 weeks do not show any obvious changes in cortical microglial or astrocyte morphology or density.** Typical immunofluorescent analysis of a) Iba1 expression (microglia) or b) GFAP expression (astrocytes) within the cerebral cortex of male C57Bl/6 mice implanted with minipumps designed to release saline vehicle (n=10) or pCS (n=7) continuously for four weeks. Nuclei are counterstained with DAPI (blue), scale bar = 30 µm.

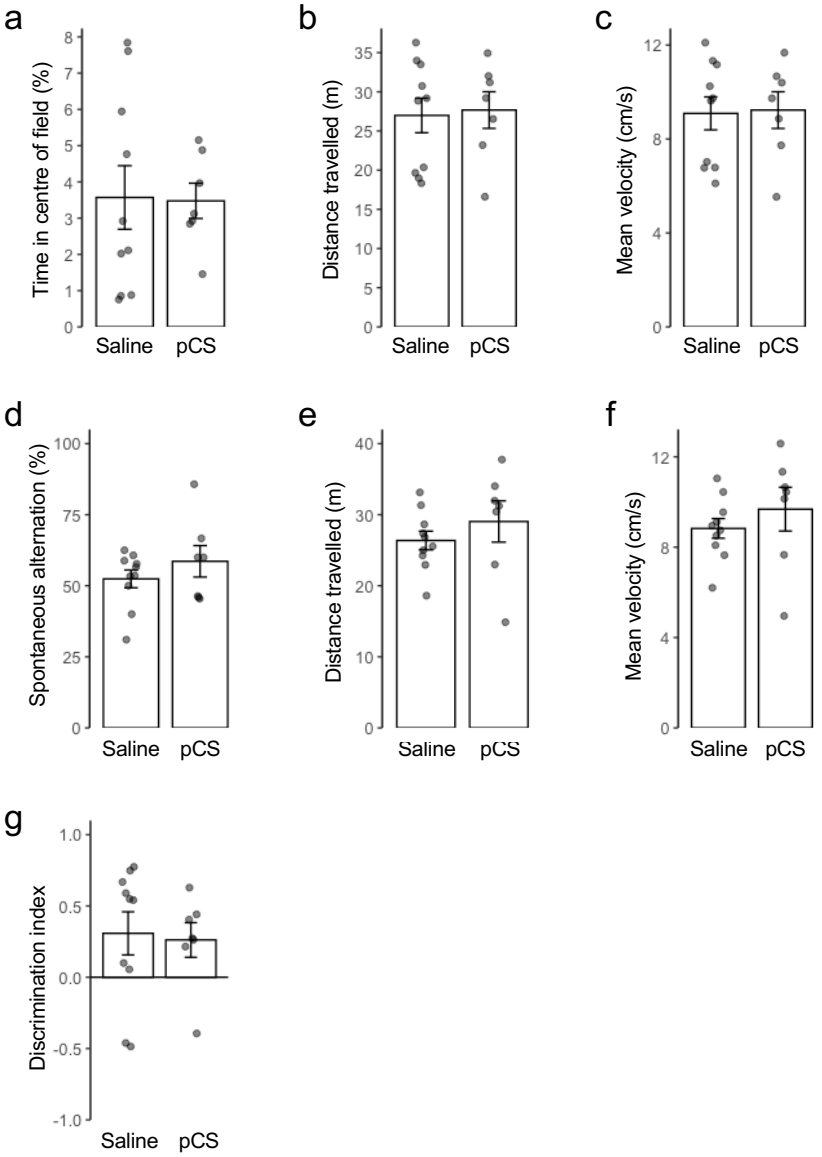


**Extended Data Figure 4: Mice exposed to raised levels of pCS for 4 weeks do not show overt behavioural changes on the open field test, Y-maze or novel object recognition task.** Mice implanted with minipumps designed to release saline vehicle or pCS continuously for four weeks were assessed for a) percentage of time in the centre zone, b) distance travelled and c) movement speed in the open field test, d) spontaneous alteration, e) distance travelled and f) mean velocity in the Y-maze task and g) discrimination index in the novel object recognition test. Data are expressed as mean ± s.e.m., *n* = 7-10 mice.

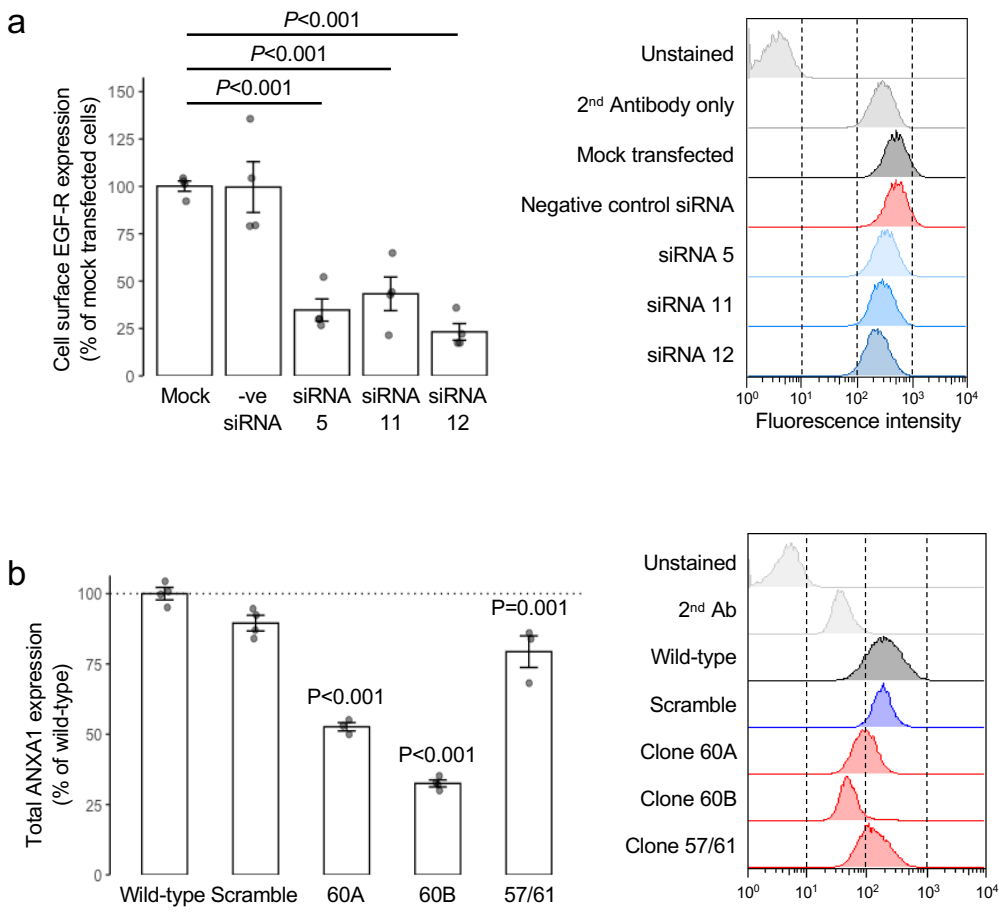


**Extended Data Figure 5: Confirmation of RNA interference knock-down experiments.** a) Transfection of hCMEC/D3 cells with siRNA sequences targeting EGFR causes a significant down-regulation of expression 96 h later when compared with mock transfected cells or cells transfected with a non-targeting negative control siRNA sequence; data are mean ± s.e.m., n = 4, representative flow cytometry histograms are shown. b) Stable transfection of hCMEC/D3 cells with shRNA sequences targeting ANXA1 causes a reduction in protein expression, an effect not seen upon transfection with a scramble shRNA sequence; data are expressed as mean ± s.e.m., *n*=4 independent experiments, representative flow cytometry histograms are shown.

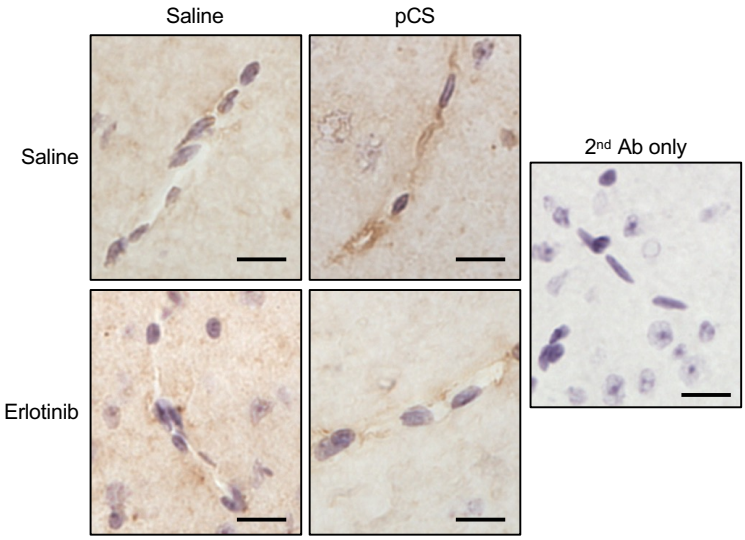


**Extended Data Figure 6: *In vivo* administration of pCS stimulates Tyr21 phosphorylation of ANXA1 in an erlotinib-sensitive manner.** Typical immunohistochemical analysis of Tyr21-phosphorylated ANXA1 expression within the cerebral microvasculature of male C57Bl/6 mice treated with pCS (10 mg/kg, i.p. 2 h) with or without erlotinib pre-treatment (50 mg/kg, i.p. 1 h pre-treatment); nuclei are counterstained with haematoxylin, scale bar = 15 µm.

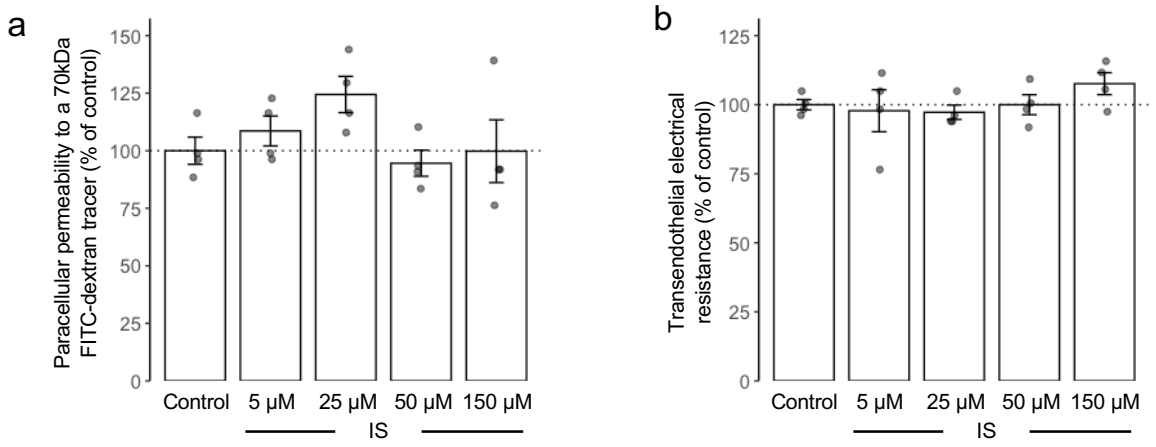


**Extended Data Figure 7: Treatment of hCMEC/D3 cells with indoxyl sulfate (IS) does not affect endothelial barrier functions at physiological or uraemia-associated concentrations.** a) Incubation of hCMEC/D3 cell monolayers with IS (5 µM, 25 µM, 50 µM, 150 µM; 24 h) did not significantly affect paracellular permeability to a 70 kDa FITC-dextran conjugate at any concentration tested; data are mean ± s.e.m., n = 4 independent experiments. b) Incubation of hCMEC/D3 cell monolayers with IS (5 µM, 25 µM, 50 µM, 150 µM; 24 h) did not significantly affect TEER at any concentration tested; data are mean ± s.e.m., n = 4 independent experiments.

**Extended Data Table 1**: Circulating concentrations (μM) of *p*-cresol and tryptophan metabolites in mice exposed for 8 weeks to pCS or saline *via* osmotic minipumps. Data are mean ± s.e.m., n=7-10, * indicates statistical significance at $P<0.05$ or less

| | **Control** | **pCS treated** | ***P*** |
|---|---|---|---|
| p-Cresol sulfate | 11.37 ± 0.89 | 38.75 ± 12.91 | 0.021* |
| p-Cresol glucuronide | 1.91 ± 0.32 | 1.21 ± 0.59 | 0.277 |
| Kynurenine | 1.57 ± 0.09 | 1.43 ± 0.09 | 0.291 |
| Tryptophan | 44.62 ± 2.37 | 40.76 ± 3.29 | 0.344 |
| Indoxyl sulfate | 7.51 ± 1.20 | 7.67 ± 1.74 | 0.938 |
| Anthranilic acid | 0.20 ± 0.05 | 0.16 ± 0.03 | 0.590 |
| Kynurenic acid | 0.21 ± 0.03 | 0.26 ± 0.09 | 0.582 |
| Indole-3-acetic acid | 0.31 ± 0.06 | 0.41 ± 0.09 | 0.352 |
| Indole-3-propionic acid | 0.64 ± 0.13 | 0.71 ± 0.15 | 0.726 |
| Indole-3-lactic acid | 1.77 ± 0.27 | 2.37 ± 0.55 | 0.300 |

## References


1. Marchesi, J. R. *et al.* The gut microbiota and host health: A new clinical frontier. *Gut* **65**, 330–339 (2016).
2. Sarkar, A. *et al.* The Microbiome in Psychology and Cognitive Neuroscience. *Trends Cogn. Sci.* **22**, 611–636 (2018).
3. Chakrabarti, A. *et al.* The microbiota-gut-brain axis: pathways to better brain health. Perspectives on what we know, what we need to investigate and how to put knowledge into practice. *Cell. Mol. Life Sci. CMLS* **79**, 80 (2022).
4. Forsythe, P., Bienenstock, J. & Kunze, W. A. Vagal pathways for microbiome-brain-gut axis communication. *Adv. Exp. Med. Biol.* **817**, 115–133 (2014).
5. Powell, N., Walker, M. M. & Talley, N. J. The mucosal immune system: master regulator of bidirectional gut–brain communications. *Nat. Rev. Gastroenterol. Hepatol.* **14**, 143–159 (2017).
6. Cani, P. D. & Knauf, C. How gut microbes talk to organs: The role of endocrine and nervous routes. *Mol. Metab.* **5**, 743–752 (2016).
7. Connell, E. *et al.* Microbial-derived metabolites as a risk factor of age-related cognitive decline and dementia. *Mol. Neurodegener.* **17**, 43 (2022).
8. Braniste, V. *et al.* The gut microbiota influences blood-brain barrier permeability in mice. *Sci. Transl. Med.* **6**, 263ra158-263ra158 (2014).
9. Hoyles, L. *et al.* Microbiome–host systems interactions: Protective effects of propionate upon the blood–brain barrier. *Microbiome* **6**, 55 (2018).
10. Hoyles, L. *et al.* Regulation of blood–brain barrier integrity by microbiome-associated methylamines and cognition by trimethylamine N-oxide. *Microbiome* **9**, 235 (2021).
11. Saito, Y., Sato, T., Nomoto, K. & Tsuji, H. Identification of phenol- and p-cresol-producing intestinal bacteria by using media supplemented with tyrosine and its metabolites. *FEMS Microbiol. Ecol.* **94**, 125 (2018).
12. Gryp, T. *et al.* Gut microbiota generation of protein-bound uremic toxins and related metabolites is not altered at different stages of chronic kidney disease. *Kidney Int.* **97**, 1230–1242 (2020).
13. Ramakrishna, B. S. *et al.* Estimation of phenolic conjugation by colonic mucosa. *J. Clin. Pathol.* **42**, 620–623 (1989).
14. Rong, Y. & Kiang, T. K. L. Characterizations of human udp-glucuronosyltransferase enzymes in the conjugation of p-cresol. *Toxicol. Sci.* **176**, 285–296 (2020).
15. Gryp, T., Vanholder, R., Vaneechoutte, M. & Glorieux, G. p-Cresyl Sulfate. *Toxins* **9**, (2017).
16. Ni, J. *et al.* In Vivo Kinetics of the Uremic Toxin P-Cresyl Sulfate in Mice With Variable Renal Function. *Ther. Apher. Dial.* **18**, 637–642 (2014).
17. Meert, N. *et al.* Novel method for simultaneous determination of p-cresylsulphate and p-cresylglucuronide: Clinical data and pathophysiological implications. *Nephrol. Dial. Transplant.* **27**, 2388–2396 (2012).
18. Sirich, T. L. Obstacles to reducing plasma levels of uremic solutes by hemodialysis. *Semin. Dial.* **30**, 403–408 (2017).
19. Liabeuf, S. *et al.* Free p-cresylsulphate is a predictor of mortality in patients at different stages of chronic kidney disease. *Nephrol. Dial. Transplant.* **25**, 1183–1191 (2010).
20. Glorieux, G. *et al.* Free p-cresyl sulfate shows the highest association with cardiovascular outcome in chronic kidney disease. *Nephrol. Dial. Transplant. Off. Publ. Eur. Dial. Transpl. Assoc. - Eur. Ren. Assoc.* **36**, 998–1005 (2021).

21. Weiner, D. E. *et al.* Cognitive Function and Kidney Disease: Baseline Data From the Systolic Blood Pressure Intervention Trial (SPRINT). *Am. J. Kidney Dis.* **70**, 357–367 (2017).
22. Ghoshal, S. & Freedman, B. I. Mechanisms of Stroke in Patients with Chronic Kidney Disease. *Am. J. Nephrol.* **50**, 229–239 (2019).
23. El Husseini, N. *et al.* Renal Dysfunction is Associated with Poststroke Discharge Disposition and In-Hospital Mortality: Findings from Get with the Guidelines-Stroke. *Stroke* **48**, 327–334 (2017).
24. O'Lone, E. *et al.* Identifying critically important cardiovascular outcomes for trials in hemodialysis: an international survey with patients, caregivers and health professionals. *Nephrol. Dial. Transplant.* **35**, 1761–1769 (2020).
25. Lau, W. L. *et al.* Chronic Kidney Disease Increases Cerebral Microbleeds in Mouse and Man. *Transl. Stroke Res.* (2019) doi:10.1007/s12975-019-00698-8.
26. Chai, C. *et al.* Increased number and distribution of cerebral microbleeds is a risk factor for cognitive dysfunction in hemodialysis patients a longitudinal study. *Med. U. S.* **95**, e2974 (2016).
27. Tan, X. *et al.* p-Cresyl Sulfate Predicts Ischemic Stroke among Patients on Hemodialysis: A Prospective Cohort Study. *Dis. Markers* **2022**, 1358419 (2022).
28. Tang, W.-H. *et al.* Protein-bounded uremic toxin p-cresylsulfate induces vascular permeability alternations. *Histochem. Cell Biol.* **149**, 607–617 (2018).
29. Gross, P. *et al.* Para-cresyl sulfate acutely impairs vascular reactivity and induces vascular remodeling. *J. Cell. Physiol.* **230**, 2927–2935 (2015).
30. Weksler, B., Romero, I. A. & Couraud, P.-O. The hCMEC/D3 cell line as a model of the human blood brain barrier. *Fluids Barriers CNS* **10**, 16 (2013).
31. Fanali, G. *et al.* Human serum albumin: from bench to bedside. *Mol. Aspects Med.* **33**, 209–290 (2012).
32. Koppe, L. *et al.* p-Cresyl glucuronide is a major metabolite of p-cresol in mouse: in contrast to p-cresyl sulphate, p-cresyl glucuronide fails to promote insulin resistance. *Nephrol. Dial. Transplant.* **32**, 2000–2009 (2017).
33. Xie, Z. *et al.* Gene Set Knowledge Discovery with Enrichr. *Curr. Protoc.* **1**, e90 (2021).
34. Sun, C.-Y. C.-Y. *et al.* Protein-Bound Uremic Toxins Induce Tissue Remodeling by Targeting the EGF Receptor. *J. Am. Soc. Nephrol.* **26**, 281–290 (2015).
35. Futter, C. E., Felder, S., Schlessinger, J., Ullrich, A. & Hopkins, C. R. Annexin I is phosphorylated in the multivesicular body during the processing of the epidermal growth factor receptor. *J. Cell Biol.* **120**, 77–83 (1993).
36. Cristante, E. *et al.* Identification of an essential endogenous regulator of blood-brain barrier integrity, and its pathological and therapeutic implications. *Proc. Natl. Acad. Sci. U. S. A.* **110**, 832–841 (2013).
37. Colamatteo, A. *et al.* Reduced Annexin A1 Expression Associates with Disease Severity and Inflammation in Multiple Sclerosis Patients. *J. Immunol.* **203**, 1753–1765 (2019).
38. Erdogan, F. *et al.* JAK-STAT core cancer pathway: An integrative cancer interactome analysis. *J. Cell. Mol. Med.* **26**, 2049–2062 (2022).
39. Xie, T. X. *et al.* Stat3 activation regulates the expression of matrix metalloproteinase-2 and tumor invasion and metastasis. *Oncogene* **23**, 3550–3560 (2004).
40. Rempe, R. G., Hartz, A. M. S. & Bauer, B. Matrix metalloproteinases in the brain and blood-brain barrier: Versatile breakers and makers. *J. Cereb. Blood Flow Metab.* **36**, 1481–1507 (2016).

41. Parrish, A. R. Matrix Metalloproteinases in Kidney Disease: Role in Pathogenesis and Potential as a Therapeutic Target. *Prog. Mol. Biol. Transl. Sci.* **148**, 31–65 (2017).
42. Jansen, J. *et al.* Remote sensing and signaling in kidney proximal tubules stimulates gut microbiome-derived organic anion secretion. *Proc. Natl. Acad. Sci. U. S. A.* **116**, 16105–16110 (2019).
43. Murray, A. M. *et al.* The Brain in Kidney Disease (BRINK) Cohort Study: Design and Baseline Cognitive Function. *Am. J. Kidney Dis. Off. J. Natl. Kidney Found.* **67**, 593–600 (2016).
44. Chronic Kidney Disease Prognosis Consortium *et al.* Association of estimated glomerular filtration rate and albuminuria with all-cause and cardiovascular mortality in general population cohorts: a collaborative meta-analysis. *Lancet Lond. Engl.* **375**, 2073–2081 (2010).
45. Toyoda, K. Cerebral small vessel disease and chronic kidney disease. *J. Stroke* **17**, 31–37 (2015).
46. Chen, S.-C., Huang, S.-Y., Wu, C.-C. & Hsu, C.-F. P-Cresylsulfate, the Protein-Bound Uremic Toxin, Increased Endothelial Permeability Partly Mediated by Src-Induced Phosphorylation of VE-Cadherin. *Toxins* **12**, E62 (2020).
47. Fang, C. *et al.* Chronic kidney disease promotes cerebral microhemorrhage formation. *J. Neuroinflammation* **20**, 51 (2023).
48. Rossi, M. *et al.* Uraemic toxins and cardiovascular disease across the chronic kidney disease spectrum: an observational study. *Nutr. Metab. Cardiovasc. Dis. NMCD* **24**, 1035–1042 (2014).
49. Lenglet, S., Montecucco, F. & Mach, F. Role of matrix metalloproteinases in animal models of ischemic stroke. *Curr. Vasc. Pharmacol.* **13**, 161–166 (2015).
50. Crosnier, A. *et al.* Renal Safety Profile of EGFR Targeted Therapies: A Study from VigiBase® the WHO Global Database of Individual Case Safety Reports. *Cancers* **13**, 5907 (2021).
51. Wardlaw, J. M. *et al.* Blood-brain barrier failure as a core mechanism in cerebral small vessel disease and dementia: evidence from a cohort study. *Alzheimers Dement.* **13**, 634–643 (2017).
52. Lau, W. L., Huisa, B. N. & Fisher, M. The Cerebrovascular-Chronic Kidney Disease Connection: Perspectives and Mechanisms. *Transl. Stroke Res.* **8**, 67–76 (2017).
53. Rosell, A. *et al.* Increased brain expression of matrix metalloproteinase-9 after ischemic and hemorrhagic human stroke. *Stroke J. Cereb. Circ.* **37**, 1399–406 (2006).
54. Muradashvili, N., Benton, R. L., Saatman, K. E., Tyagi, S. C. & Lominadze, D. Ablation of matrix metalloproteinase-9 gene decreases cerebrovascular permeability and fibrinogen deposition post traumatic brain injury in mice. *Metab. Brain Dis.* **30**, 411–426 (2015).
55. Zhao, J. *et al.* Relationship between MMP-9 serum levels and tHcy levels and total imaging load and cognitive dysfunction. *J. Stroke Cerebrovasc. Dis. Off. J. Natl. Stroke Assoc.* **31**, 106759 (2022).
56. Matsuki, H. *et al.* Chronic kidney disease causes blood-brain barrier breakdown via urea-activated matrix metalloproteinase-2 and insolubility of tau protein. *Aging* **15**, 10972–10995 (2023).
57. Zakiyanov, O., Kalousová, M., Zima, T. & Tesař, V. Matrix metalloproteinases and tissue inhibitors of matrix metalloproteinases in kidney disease. *Adv. Clin. Chem.* **105**, 141–212 (2021).
58. Nation, D. A. *et al.* Blood-brain barrier breakdown is an early biomarker of human cognitive dysfunction. *Nat. Med.* **25**, 270–276 (2019).

1061 59. Bobot, M. *et al.* Uremic Toxic Blood-Brain Barrier Disruption Mediated by AhR Activation
1062 Leads to Cognitive Impairment during Experimental Renal Dysfunction. *J. Am. Soc.*
1063 *Nephrol. JASN* **31**, 1509–1521 (2020).
1064 60. Ahire, C. *et al.* Accelerated cerebromicrovascular senescence contributes to cognitive
1065 decline in a mouse model of paclitaxel (Taxol)-induced chemobrain. *Aging Cell* **22**, e13832
1066 (2023).
1067 61. Wang, Y. *et al.* Comparative plasma metabolomic analysis to identify biomarkers for lead-
1068 induced cognitive impairment. *Chem. Biol. Interact.* **366**, 110143 (2022).
1069 62. Barreto, F. C. *et al.* Serum indoxyl sulfate is associated with vascular disease and mortality
1070 in chronic kidney disease patients. *Clin. J. Am. Soc. Nephrol. CJASN* **4**, 1551–1558
1071 (2009).
1072 63. Vanholder, R., Nigam, S. K., Burtey, S. & Glorieux, G. What If Not All Metabolites from the
1073 Uremic Toxin Generating Pathways Are Toxic? A Hypothesis. *Toxins* **14**, 221 (2022).
1074 64. Liabeuf, S. *et al.* Does P-Cresylglucuronide Have the Same Impact on Mortality as Other
1075 Protein-Bound Uremic Toxins? *PLoS ONE* **8**, (2013).
1076 65. Stachulski, A. V., Knausenberger, T. B.-A., Shah, S. N., Hoyles, L. & McArthur, S. A host-
1077 gut microbial amino acid co-metabolite, p-cresol glucuronide, promotes blood-brain barrier
1078 integrity in vivo. *Tissue Barriers* 2073175 (2022) doi:10.1080/21688370.2022.2073175.
1079 66. Kim, D., Langmead, B. & Salzberg, S. L. HISAT: a fast spliced aligner with low memory
1080 requirements. *Nat. Methods* **12**, 357–360 (2015).
1081 67. Liao, Y., Smyth, G. K. & Shi, W. featureCounts: an efficient general purpose program for
1082 assigning sequence reads to genomic features. *Bioinforma. Oxf. Engl.* **30**, 923–930
1083 (2014).
1084 68. Love, M. I., Huber, W. & Anders, S. Moderated estimation of fold change and dispersion
1085 for RNA-seq data with DESeq2. *Genome Biol.* **15**, 550 (2014).
1086 69. Tarca, A. L. *et al.* A novel signaling pathway impact analysis. *Bioinforma. Oxf. Engl.* **25**,
1087 75–82 (2009).
1088 70. Zhang, J. D. & Wiemann, S. KEGGgraph: A graph approach to KEGG PATHWAY in R
1089 and bioconductor. *Bioinformatics* **25**, 1470–1471 (2009).
1090 71. Csárdi, G. & Nepusz, T. The igraph software package for complex network research.
1091 *InterJournal Complex Syst.* (2006).
1092 72. Mulla, A. *et al.* Expression, subcellular localization and phosphorylation status of annexins
1093 1 and 5 in human pituitary adenomas and a growth hormone-secreting carcinoma. *Clin.*
1094 *Endocrinol. (Oxf.)* **60**, 107–119 (2004).
1095 73. Denninger, J. K., Smith, B. M. & Kirby, E. D. Novel Object Recognition and Object Location
1096 Behavioral Testing in Mice on a Budget. *J. Vis. Exp. JoVE* (2018) doi:10.3791/58593.
1097 74. Weksler, B. B. *et al.* Blood-brain barrier-specific properties of a human adult brain
1098 endothelial cell line. *FASEB J. Off. Publ. Fed. Am. Soc. Exp. Biol.* **19**, 1872–4 (2005).
1099
1100